Medical Image Analysis 18 (2014) 1361–1376

Contents lists available at ScienceDirect

Medical Image Analysis

journal homepage: www.elsevier.com/locate/media

Data-driven estimation of cardiac electrical diffusivity from 12-lead ECG signals

Oliver Zettinig [a,b], Tommaso Mansi [a,*], Dominik Neumann [a,c], Bogdan Georgescu [a], Saikiran Rapaka [a], Philipp Seegerer [a,c], Elham Kayvanpour [d], Farbod Sedaghat-Hamedani [d], Ali Amr [d], Jan Haas [d], Henning Steen [d], Hugo Katus [d], Benjamin Meder [d], Nassir Navab [b], Ali Kamen [a], Dorin Comaniciu [a]

[a] Siemens Corporate Technology, Imaging and Computer Vision, Princeton, NJ, USA
[b] Computer Aided Medical Procedures, Technische Universität München, Germany
[c] Pattern Recognition Lab, Friedrich-Alexander-Universität Erlangen-Nürnberg, Germany
[d] Heidelberg University Hospital, Heidelberg, Germany

ARTICLE INFO

Article history:
Received 7 January 2014
Received in revised form 17 March 2014
Accepted 10 April 2014
Available online 26 April 2014

Keywords:
Cardiac electrophysiology
Statistical learning
Lattice-Boltzmann method
Uncertainty quantification
Electrocardiogram

ABSTRACT

Diagnosis and treatment of dilated cardiomyopathy (DCM) is challenging due to a large variety of causes and disease stages. Computational models of cardiac electrophysiology (EP) can be used to improve the assessment and prognosis of DCM, plan therapies and predict their outcome, but require personalization. In this work, we present a data-driven approach to estimate the electrical diffusivity parameter of an EP model from standard 12-lead electrocardiograms (ECG). An efficient forward model based on a mono-domain, phenomenological Lattice-Boltzmann model of cardiac EP, and a boundary element-based mapping of potentials to the body surface is employed. The electrical diffusivity of myocardium, left ventricle and right ventricle endocardium is then estimated using polynomial regression which takes as input the QRS duration and electrical axis. After validating the forward model, we computed 9500 EP simulations on 19 different DCM patients in just under three seconds each to learn the regression model. Using this database, we quantify the intrinsic uncertainty of electrical diffusion for given ECG features and show in a leave-one-patient-out cross-validation that the regression method is able to predict myocardium diffusion within the uncertainty range. Finally, our approach is tested on the 19 cases using their clinical ECG. 84% of them could be personalized using our method, yielding mean prediction errors of 18.7 ms for the QRS duration and 6.5° for the electrical axis, both values being within clinical acceptability. By providing an estimate of diffusion parameters from readily available clinical data, our data-driven approach could therefore constitute a first calibration step toward a more complete personalization of cardiac EP.

1. Introduction

1.1. Clinical rationale

With around 17.3 million deaths per year (Mendis et al., 2011), the global burden of cardiovascular diseases remains high and causes a significant social and economic impact. According to recent estimates, about 2% of adults in Europe (McMurray et al., 2012) and 2.4% of adults in the US (Roger et al., 2012) suffer from heart failure alone, with the prevalence rising to more than 10% among persons 70 years of age or older. One of the most common causes of heart failure is dilated cardiomyopathy (DCM), a condition with weakened and enlarged ventricles and atria, leading to an ineffective pump function that can directly and indirectly affect the lungs, liver, and other organ systems. The prevalence of DCM amounts to around 0.9% of adults in the US (Ferri, 2013), and the disease is the leading indication for heart transplantation in younger adults. Due to a large variety of individual causes and disease stages, diagnosis and treatment of DCM remains an open challenge.

Cardiac arrhythmia, i.e. irregular electrical activity of the heart, occurs frequently in heart failure patients, particularly in those with DCM (McMurray et al., 2012). But also beyond DCM, the prevalence of cardiac rhythm disorders has increased significantly in the last decade following an improvement in patient care (Marcus et al., 2013). Depending on the kind of rhythm disorder, which is commonly diagnosed using electrocardiography (ECG),

* Corresponding author. Address: 755 College Road East, 08540 Princeton, NJ, USA. Tel.: +1 609 734 3537; fax: +1 609 734 6565.
E-mail address: tommaso.mansi@siemens.com (T. Mansi).

http://dx.doi.org/10.1016/j.media.2014.04.011
1361-8415/

the treatment of arrhythmia includes drug therapies, radio frequency ablation and the implantation of artificial pacemakers and cardioverter-defibrillators. Unfortunately, around 30% of patients are non-responders to these invasive treatments, and in up to 50% of the cases, recurrences are identified (Auricchio et al., 2011).

As a result, tools for a more predictive assessment of cardiac electrophysiology (EP) are needed. Computational assistance is not only required for a superior patient management and diagnosis but could also benefit therapy planning, outcome prediction and intervention guidance. While improved risk stratification could help avoiding unnecessary surgeries, the potential of optimizing invasive procedures, for instance by choosing optimal electrode locations, can potentially lead to an increased success rate and fewer non-responders. For this purpose, computational models can be employed to study and evaluate patient-specific electrophysiology in silico.

1.2. Technical background: computational models of cardiac electrophysiology

1.2.1. Models of cardiac action potential

A wide range of computational models of cardiac EP with different biological scales and theoretical complexity has been proposed since the seminal work of Hodgkin and Huxley (1952). Especially in the last decade, the community has witnessed tremendous progress in modeling efforts (Clayton et al., 2011). Depending on their level of detail, EP models can be classified into three groups: Biophysical, phenomenological and Eikonal models.

Biophysical cellular models capture cardiac electrophysiology directly at cell level by describing biological phenomena responsible for myocyte depolarization and repolarization. More precisely, ionic interactions within the cell and across the cell membrane (ion channels) are considered (Noble, 1962; Luo and Rudy, 1991; Noble et al., 1998; Ten Tusscher et al., 2004) and lead to complex equations, commonly one per molecular process. Although it has been shown that biophysical models can reproduce different electrophysiological behaviors such as action potential restitution and conduction velocity, the large amount of parameters limits their usage in clinical applications due to the difficulty of personalization.

Cell models are then integrated at the organ level using reaction–diffusion partial differential equations (PDEs). Two major categories can be distinguished. While mono-domain approaches neglect interstitial effects and consider the myocardium as single excitable tissue (Coudière and Pierre, 2006), bi-domain strategies superimpose intra- and extra-cellular domains and take different electrical properties into account (Bourgault et al., 2009). In the absence of external stimuli, mono-domain models have been shown to produce almost identical results as their bi-domain counterparts (Potse et al., 2006).

Phenomonological models, historically the first models to be proposed by FitzHugh (1961), work at a more macroscopic level. Derived from experimental observations, the action potential is described by a small number of parameters with direct influence on its shape, disregarding the underlying ionic interactions (Aliev and Panfilov, 1996; Mitchell and Schaeffer, 2003). Having only few parameters with direct effect on measurable output facilitates model personalization, and the lower computational cost when compared to biophysical models offers a reasonable compromise between modeling capacity and performance. The distinction between mono-domain organ level integration schemes such as in Aliev and Panfilov (1996), Fenton and Karma (1998), Mitchell and Schaeffer (2003) and bi-domain approaches such as in Clayton and Panfilov (2008) can be applied to phenomonological models, too. Recent numerical advances based on Lattice-Boltzmann methods (Rapaka et al., 2012) or Finite Element methods (Talbot et al., 2013) exploit the massively parallel architecture of modern graphics processing units, and allow near real-time performance and user interaction.

Eikonal models (Franzone et al., 1990; Keener and Sneyd, 1998; Sermesant et al., 2007) solely concentrate on the propagation of the electrical wave to stimulate muscle activation. The formation as well as the shape of the action potential in myocytes is neglected. Governed only by the anisotropic speed of wave propagation, the local time of wave arrival throughout the myocardium, can be computed very efficiently using fast marching methods (Sethian, 1999; Wallman et al., 2012). While it has become possible to simulate wave reentry phenomena with Eikonal models (Pernod et al., 2011), capturing other complex pathological conditions such as arrhythmias, fibrillations or tachycardia is more challenging.

1.2.2. Model personalization

In order to apply the aforementioned EP models in clinical settings, patient-specific physiology has to be captured by personalized model parameters. Finding those is challenging in the clinical workflow as the estimation from patient data implies solving an inverse problem. In this context, the *forward model* denotes the computation of the electrical wave propagation from the heart to the point of measurement (catheter electrode, body surface), and the *inverse model* the back-projection of measurement data onto the heart and the inference of model parameters (Gulrajani, 1998).

Inverse problem techniques are computationally demanding because they comprise an optimization problem and therefore require a large quantity of forward model runs (Modre et al., 2002; Chinchapatnam et al., 2008; Dössel et al., 2011). Alternatively, data-driven algorithms have been investigated to tackle model personalization. Linking activation patterns with the resulting cardiac motion that can be observed in clinical images, Prakosa et al. (2013) train a machine-learning algorithm to estimate depolarization times for cardiac segments from regional kinematic descriptors. Jiang et al. (2011) apply statistical learning to map body surface potentials onto the epicardium. Konukoglu et al. (2011) derive a surrogate EP model based on polynomial chaos theory to personalize an Eikonal model. Wallman et al. (2014) infer tissue conduction properties using Bayesian inference to be patient-specific. The advantage of these statistical methods is the possibility to quantify uncertainty and to optimize the location of measurements. Machine learning techniques could therefore constitute efficient strategies for model personalization. However, a sufficient sampling of the parameter space is needed for these approaches to yield meaningful results. In this study, we aim to achieve an estimation of model parameters only from sparse electrocardiogram data.

1.2.3. Models of electrocardiogram and torso potential

From the perspective of data acquisition, endocardial mapping (Sermesant et al., 2009; Relan et al., 2011) facilitates the parameter estimation as it provides dense potential measurements but it is pre-operatively often avoided as it is invasive. A non-invasive alternative is to back-project electrical potentials measured at the body surface in the form of electrocardiograms (ECG), to the epicardium. Considering the ill-posedness of the parameter estimation, the use of body surface mapping (BSM) has been investigated (Dössel et al., 2011; Wang et al., 2011; Han et al., 2013). In contrast to standard 12-lead ECG, BSM is however not yet widely available as diagnostic modality.

If body surface ECG data is used for parameter estimation, regardless of the number of traces, a model of electrical potentials at the surface of the torso is needed. In terms of the forward model, current approaches employ both Finite Element (FEM) and Boundary Element (BEM) methods. While the former intrinsically

allow varying conductivity within and across different organs (Li et al., 2007; Geneser et al., 2008; Liu et al., 2012), the latter either assume constant isotropic conductivity throughout the entire torso (Barr et al., 1977; Shou et al., 2009) or integrate additional surface meshes delineating neighboring organs (Potse et al., 2009). Furthermore, in a numerical study by Boulakia et al. (2010), decoupling the computation of cardiac electrophysiology and body surface potentials has been shown to preserve the shape of ECG features well.

1.3. Aim of the study

The personalization of computational EP models, i.e. the estimation of patient-specific model parameters, remains challenging because of lack of dense data and the ill-posedness of the inverse problem. We therefore propose in this work to estimate EP model parameters from standard 12-lead electrocardiograms (ECG) only using a data-driven method that provides insight into estimation uncertainty. In particular, our method is based on statistical learning and employs polynomial regression to map ECG features to model parameters, instead of finding a solution of the inverse problem numerically. The key contributions of this work are:

i. A fast forward model of cardiac electrophysiology and electrocardiogram based on a Lattice-Boltzmann formulation and the boundary element method.
ii. A novel data-driven approach to automatically and efficiently estimate heart electrical diffusivity from 12-lead ECG features.
iii. The quantification of the intrinsic uncertainty of the inverse problem, i.e. the uncertainty of myocardial diffusion given a set of ECG features, through statistical learning.
iv. The evaluation of our estimation framework on 19 DCM cases.

This study extends our previous work (Zettinig et al., 2013a) as follows:

i. In a detailed quantitative evaluation and convergence analysis of the employed forward model and its parts, we show the influence of various model parameters on the ECG features.
ii. Results of benchmark experiments allow insights on the computational performance of our approach.
iii. A comparison with other statistical learning techniques justifies the choice of multivariate polynomial regression.
iv. For a quantitative evaluation of the diffusion estimation method, we use a significantly more extensive dataset of synthetic and real case data, allowing to capture a bigger variety of individual physiologies.

2. Methods

This section presents the details of the proposed data-driven EP parameter estimation framework. Section 2.1 describes how a patient-specific anatomical model is derived from clinical images. In Section 2.2, a fast forward model of cardiac electrophysiology, body surface potentials and electrocardiogram, as shown in Fig. 1, is detailed. Thereafter, Section 2.3 describes the proposed data-driven diffusion estimation procedure. Implementation details are reported in Section 2.4.

2.1. Patient-specific model of cardiac anatomy

The complete workflow of anatomical model generation is depicted in Fig. 2. First, we employ the framework presented in Zheng et al. (2008) to automatically estimate, under expert guidance, heart morphology from cine magnetic resonance images (MRI). For anatomical structure localization, the Marginal Space Learning (MSL) framework intuitively finds control points representing important landmarks such as valves and ventricular septum cusps using Haar- and steerable features. Then, a point-distribution model of biventricular geometry is mapped to these control points and successively deformed according to learning-based boundary delineation through a Probabilistic Boosting Tree (PBT). Using a manifold-based motion model, the resulting surface meshes are tracked over the cardiac sequence such that point correspondences are maintained. To form a closed surface mesh of the biventricular myocardium, the segmented triangulations of the epicardium and endocardia are fused together. The myocardium at end-diastole is finally mapped onto a Cartesian grid with isotropic spacing and represented as a level-set.

Based on the original segmentation meshes and point-to-point distances, we consider five domains in our anatomical model: The left and right ventricular septum, which mimics the His bundle and serves as initialization zone of the electrophysiological wave, the left and right endocardia mimicking the Purkinje system of fast electrical diffusivity, and finally the myocardium with slower diffusivity.

As diffusion tensor imaging (DTI) is not yet clinically available (Wu et al., 2009), the rule-based strategy described by Bayer et al. (2012) is extended as proposed by Zettinig et al. (2013b) to compute a generic model of myocardium fiber architecture. Below the basal plane, identified automatically using the point correspondences of the initial triangulations, the fiber elevation angle α_f is assigned to all grid nodes. Defined as the angle with respect to the short axis, α_f varies linearly across the myocardium from -70° on the epicardium to $+70^\circ$ on the endocardium. Around the valves, fiber directions are fixed (longitudinal around the aortic valve, tangential otherwise), and between the basal plane and the valves finally interpolated first following the myocardium surface, then transmurally (Moireau, 2008; Zettinig et al., 2013b). All interpolations throughout the myocardium rely on geodesic distances and the Log-Euclidean framework (Arsigny et al., 2006). Fig. 2 illustrates the myocardium fiber model and the electrophysiology zones.

A body surface triangulation is obtained using a manual, two-step procedure. First, the contours of the torso are outlined in coronal, sagittal and transverse slices of the survey MR image, and visualized together with the heart model. Second, a manual affine registration of an atlas of torso geometry to the contours is performed as illustrated in Fig. 3. The atlas is obtained from a full-body CT dataset of a subject within normal weight range.

2.2. Fast forward model of cardiac electrocardiogram

Our forward model consists of three sequential steps described in the following sections (Fig. 1). First, we compute cardiac electrophysiology using the LBM-EP algorithm proposed by Rapaka et al. (2012). Second, we estimate extracellular potentials at the epicardium using an elliptic formulation and project them to the torso by means of a Boundary Element Method technique. Ultimately, ECG traces are computed and ECG features automatically calculated.

2.2.1. LBM-EP: Lattice-Boltzmann model of myocardium transmembrane potentials

Cardiac EP is computed according to the phenomenological mono-domain model proposed by Mitchell and Schaeffer (2003), which describes the normalized transmembrane potential (TMP) $v(t) \in [0,1]$ throughout the myocardium with the following equation:

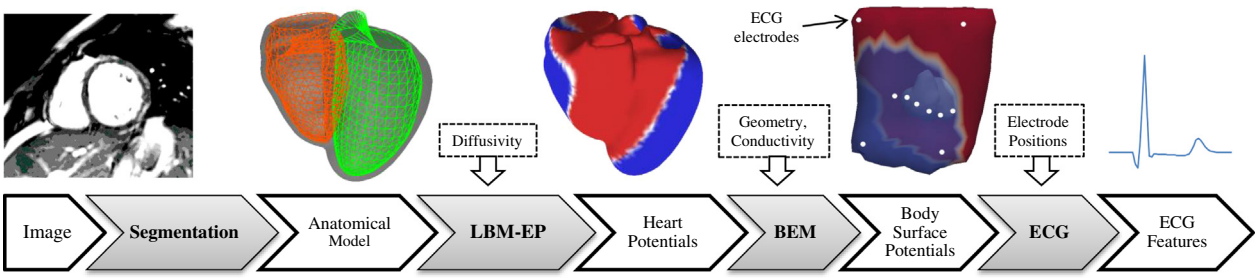

Fig. 1. Steps of proposed forward model of ECG.

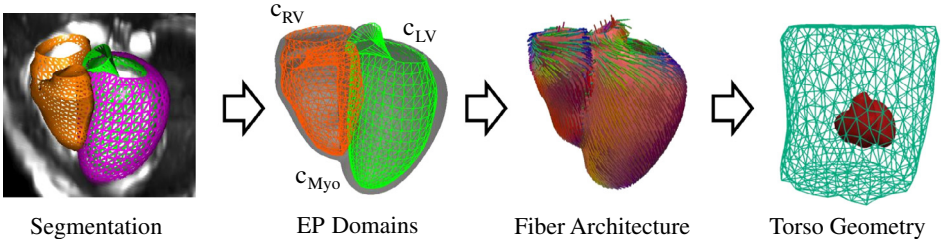

Fig. 2. Workflow of anatomical model generation. *See text for details.*

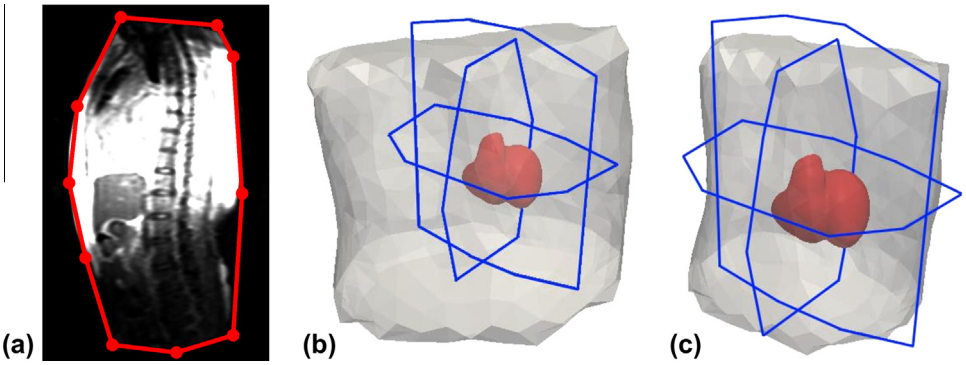

Fig. 3. (a) Sagittal image slice and manually outlined contour. (b) Atlas of torso geometry before registration and (c) after manual registration to body contours in coronal, sagittal and transverse image slices.

$$\frac{\partial v}{\partial t} = J_{in} + J_{out} + J_{stim} + c\nabla \cdot \mathrm{D}\nabla v \tag{1}$$

Electrical diffusion is formulated anisotropically with the diffusion coefficient c and the anisotropy ratio ρ, defining the anisotropic diffusion tensor $\mathrm{D} = \rho \mathrm{I} + (1-\rho)\mathbf{f}\mathbf{f}^{\mathrm{T}}$ with $\mathbf{f}$ denoting the fiber direction. The EP zones as defined in Section 2.1 are assigned three different diffusion coefficients: c_{LV} and c_{RV} for the left and right endocardium, respectively (fast conducting Purkinje network), and c_{Myo} for the myocardium.

The model simplifies all ion channel interactions to only an inward current J_{in} and an outward current J_{out} (Eqs. (2) and (3)). The former captures the fast acting ionic currents in the myocyte and depends on the gating variable $h(t)$ that models the state of the ion channels.

$$J_{in} = \frac{h(t)v^2(1-v)}{\tau_{in}}, \quad \text{with } \frac{dh}{dt} = \begin{cases} \frac{1-h}{\tau_{open}}, & \text{if } v < v_{gate} \\ \frac{-h}{\tau_{close}}, & \text{otherwise} \end{cases} \tag{2}$$

$$J_{out} = \frac{-v}{\tau_{out}} \tag{3}$$

The time constants $\tau_{in} \ll \tau_{out} \ll \tau_{open}, \tau_{close}$ are directly related to the shape and duration of the action potential, allowing for personalization from clinical data. As illustrated in Fig. 4, τ_{close} relates to the action potential duration (APD), for which a linear transmural gradient as described by Glukhov et al. (2010) is employed. The remaining model parameters, including the change-over voltage v_{gate}, are obtained from literature (Mitchell and Schaeffer, 2003) and kept constant throughout the myocardium. Table 1 lists all fixed model parameters.

The complex PDE (Eq. 1) is solved using the LBM-EP algorithm, an efficient Lattice-Boltzmann method, proposed by Rapaka et al. (2012). It should be noted, though, that the LBM-EP algorithm is generic and would allow any mono-domain cell model to be solved. In short, the method maintains a vector of distribution functions $\mathbf{f}(\mathbf{x}) = \{f_i(\mathbf{x})\}_{i=1\ldots7}$, where $f_i(\mathbf{x})$ represents the probability of finding a particle traveling along the edge $\mathbf{e}_i$ of node $\mathbf{x}$. The seven indices correspond to the central position and the six principal connections on the Cartesian grid, respectively. Its computation is decomposed into two consecutive steps, namely the *collision* phase, yielding intermediate post-collision states f_i^* and the *streaming* phase, propagating the distribution functions along their corresponding edges:

$$f_i^* = f_i - A_{ij}(f_j - \omega_j v) + \delta t \omega_i (J_{in} + J_{out} + J_{stim}), \tag{4}$$

$$f_i(\mathbf{x} + \mathbf{e}_i, t + \delta t) = f_i^*(\mathbf{x}, t) \tag{5}$$

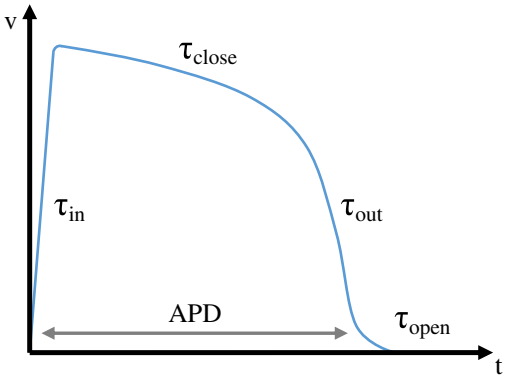

Fig. 4. Four stages of the myocyte action potential and the relating parameters of the Mitchell-Schaeffer model.

Table 1
Parameters used for the Mitchell-Schaeffer model (Mitchell and Schaeffer, 2003; Glukhov et al., 2010). Note that v_{gate} is dimensionless because $v(t)$ is normalized to $[0,1]$.

Parameter	
v_{gate}	0.13
τ_{in}	0.3 ms
τ_{out}	6 ms
τ_{open}	120 ms
$\tau_{close_{endo}}$	130 ms
$\tau_{close_{epi}}$	90 ms

The collision matrix $A = (A_{ij})$ relaxes the distribution function f_i toward the local value of the potential v and is defined such that anisotropic fiber-related diffusion is taken into account. The weighting factors ω_i are utilized to emphasize the center position. We refer the reader to Rapaka et al. (2012) for further details. Using a forward Euler scheme, the gating variable $h(t)$ can easily be updated at every node. Eventually, the transmembrane potential $v(\mathbf{x},t)$ is defined as the sum of the distribution functions: $v(\mathbf{x},t) = \sum_i f_i(\mathbf{x},t)$ and transferred to the range $[-70\,\text{mV}, 30\,\text{mV}]$ using the scaling factors given in Mitchell and Schaeffer (2003). The depolarization times $T_d(\mathbf{x})$ are obtained as the points in time when the potential first exceeds the change-over voltage:

$$T_d(\mathbf{x}) = \arg\min_t \{ v(\mathbf{x},t) \geqslant v_{gate} \} \tag{6}$$

2.2.2. Boundary element model of torso potentials

For the propagation of electrical potentials through the body, it is necessary to estimate cardiac extracellular potentials $\phi_e(t)$ from the TMP $v(t)$. To that end, we employ the elliptic formulation proposed by Chhay et al. (2012), which assumes a constant diffusion anisotropy ratio $\lambda = c_i(\mathbf{x})/c_e(\mathbf{x})$, with c_i and c_e denoting the intra- and extracellular diffusion coefficients respectively. Within the entire myocardium domain Ω, the extracellular potential ϕ_e is expressed as:

$$\phi_e(\mathbf{x},t) = \frac{\lambda}{1+\lambda}\frac{1}{|\Omega|}\int_\Omega (v(\mathbf{y},t) - v(\mathbf{x},t))d\mathbf{y} \tag{7}$$

Next, we utilize a boundary element method (BEM) as described in Barr et al. (1977) and refined in Shou et al. (2009) to project the potentials ϕ_e from the epicardium to the torso. Before, tri-linear interpolation is used to map ϕ_e from the Cartesian grid back to the epicardial surface mesh. Following Green's second identity, the potential $\phi(\mathbf{x})$ at any observation point $\mathbf{x}$ of the thoracic domain is given as:

$$\phi(\mathbf{x}) = \frac{1}{4\pi}\int_{S_B} \phi_B \frac{\mathbf{r}\cdot\mathbf{n}}{||\mathbf{r}||^3} dS_B + \frac{1}{4\pi}\int_{S_H}\left[\phi_e\frac{\mathbf{r}\cdot\mathbf{n}}{||\mathbf{r}||^3} + \frac{\nabla\phi_e\cdot\mathbf{n}}{||\mathbf{r}||}\right] dS_H \tag{8}$$

Hereby, subscripts B denote the body surface and the potentials thereupon, S_H the epicardial heart surface. The surface normals $\mathbf{n}$ face outward of the domain under consideration (i.e. outward at the torso and inward at the epicardium). $\mathbf{r}$ is defined as the vector from $\mathbf{x}$ to the point of integration as illustrated in Fig. 5a. Note that Eq. (8) assumes that $\nabla\phi_B = 0$.

After placing the observation point $\mathbf{x}$ only onto the two surfaces, discretization in triangular meshes, and reformulation in matrix form, a system of linear equations can be constructed (Barr et al., 1977):

$$\mathrm{P}_{BB}\phi_B + \mathrm{P}_{BH}\phi_e + \mathrm{G}_{BH}\Gamma_H = 0 \tag{9}$$

$$\mathrm{P}_{HB}\phi_B + \mathrm{P}_{HH}\phi_e + \mathrm{G}_{HH}\Gamma_H = 0 \tag{10}$$

Obtaining the geometric coefficients of matrices P and G requires the evaluation of two integrals. The integral $\int(\mathbf{r}\cdot\mathbf{n})/||\mathbf{r}||^3 dS$ in fact describes the solid angle $d\Omega$ subtended at any observation point by a surface element dS (see Fig. 5b), and can be efficiently computed with the following closed form formula (Van Oosterom and Strackee, 1983):

$$\tan\frac{d\Omega}{2} = \frac{\mathbf{a}_1\cdot(\mathbf{a}_2\times\mathbf{a}_3)}{\prod_{i=1}^3\|\mathbf{a}_i\| + \|\mathbf{a}_1\|(\mathbf{a}_2\cdot\mathbf{a}_3) + \|\mathbf{a}_2\|(\mathbf{a}_3\cdot\mathbf{a}_1) + \|\mathbf{a}_3\|(\mathbf{a}_1\cdot\mathbf{a}_2)} \tag{11}$$

Hereby, vectors $\mathbf{a}_i$ denote the vectors from the observation point to the three vertices of the triangulated surface element dS. The surface-over-distance integral $\int dS/\mathbf{r}$, on the other hand, is solved using Gaussian quadrature. Canceling out the matrix Γ_H, which contains the gradients $\nabla\phi_e$, a precomputable transfer matrix that entirely depends on the geometry can be defined:

$$\mathrm{Z}_{BH} = \left(\mathrm{P}_{BB} - \mathrm{G}_{BH}\mathrm{G}_{HH}^{-1}\mathrm{P}_{HB}\right)^{-1}\left(\mathrm{G}_{BH}\mathrm{G}_{HH}^{-1}\mathrm{P}_{HH} - \mathrm{P}_{BH}\right) \tag{12}$$

This allows to express body surface potentials by means of a simple matrix multiplication: $\phi_B = \mathrm{Z}_{BH}\phi_e$.

2.2.3. Electrocardiogram calculation

From the potentials ϕ_B at the torso, the standard Einthoven, Goldberger and Wilson leads (Chung, 1989) are computed. For the sake of simplicity, electrode positions were chosen to coincide with manually selected torso mesh vertex positions.

In this work, we focus on two meaningful ECG features. On the one hand, the duration of the QRS complex Δ_{QRS} is dependent on the total time the electrical wave requires to propagate throughout the entire myocardium. On the other hand, the mean electrical axis angle α is suited to detect imbalances between left and right ventricular wave conduction. From the computed ECG signals, Δ_{QRS} and α are derived as follows:

- For numerical stability, the QRS complex is detected using the depolarization times computed by LBM-EP. Assuming one full heart cycle, it is computed as follows: $\Delta_{QRS} = \max_x T_d(\mathbf{x}) - \min_x T_d(\mathbf{x})$.
- The electrical axis is computed using the Einthoven leads I and II: $\alpha = \arctan\left[(2h_{II} - h_I)/(\sqrt{3}h_I)\right]$, where the h_i's are the sum of the automatically detected R and S peak amplitudes (minimum and maximum) in the respective leads during the QRS complex.

2.3. Data-driven estimation of myocardium EP diffusion

The forward model as described above can be seen as a dynamic system $\mathbf{y} = f(\boldsymbol{\theta})$ with the diffusion coefficients $\boldsymbol{\theta} = (c_{Myo}, c_{LV}, c_{RV})$ as

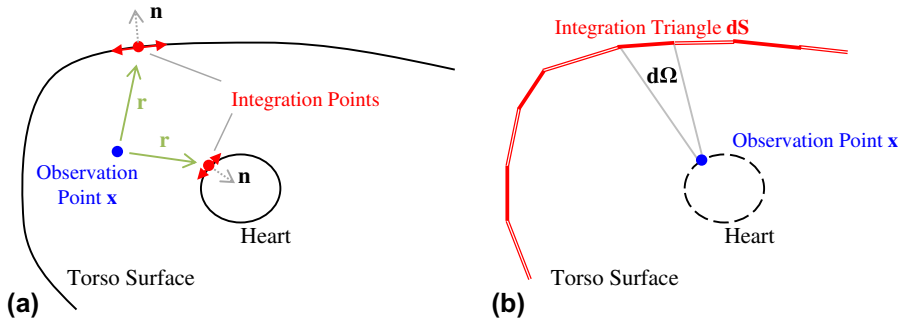

Fig. 5. (a) For any given observation point in the thoracic domain, both torso and heart surfaces need to be integrated as defined in Eq. (8). (b) After discretization, geometric coefficients of the P matrices in Eq. (10) require the evaluation of solid angles.

free parameters and the ECG features $\mathbf{y} = (\Delta_{QRS}, \alpha)$ as outputs of the system. Estimating diffusion parameters from ECG features therefore consists in evaluating a function $g(\mathbf{y})$ that approximates the inverse problem $\boldsymbol{\theta} = g(\mathbf{y}) \approx f^{-1}(\mathbf{y})$, as shown in Fig. 6. In contrast to solving the inverse problem numerically using an optimization strategy such as Dössel et al. (2011), we propose to learn the inverse function instead.

The ECG features Δ_{QRS} and α vary significantly within the population, even in healthy subjects, due to a variety of factors including heart morphology and position. To cope with this geometrical variety, our algorithm scouts the parameter space using three forward model runs with the predefined diffusion coefficients listed in Table 2. The resulting ECG features are then used for an effective normalization scheme, intrinsically considering geometrical features of a particular patient:

- Configuration F_1 contains nominal EP diffusion parameters and thus entails a normal wave propagation. Provided the same diffusivity, the electrical wave will take longer to propagate through the entire myocardium in larger hearts, which is why we use $\Delta_{QRS_{F_1}}$ to normalize the QRS duration: $\overline{\Delta_{QRS}} = \Delta_{QRS}/\Delta_{QRS_{F_1}}$.
- The other two configurations contain extremely low LV and RV diffusivity (LBBB-like scenario: F_2; RBBB-like scenario: F_3). The obtained electrical axis parameters α_{F_2} and α_{F_3} scout the patient-specific space of axis deviation, because we assume that the vast majority of forward model runs with arbitrary physiological diffusion coefficients will yield an electrical axis between them: $\alpha_{F_2} \leqslant \alpha \leqslant \alpha_{F_3}$. Therefore, we perform normalization as follows: $\overline{\alpha} = (\alpha - \alpha_{F_2})/(\alpha_{F_3} - \alpha_{F_2})$.

Note that our normalization scheme does not lead to the same numerical ranges of $\overline{\Delta_{QRS}}$ and $\overline{\alpha}$. The purpose of the normalization is only to compensate for inter-patient variability; the regression framework will cope with scaling of the input values. Finally, multivariate polynomial regression of degree N is employed to learn the model $\boldsymbol{\theta} = g(\overline{\Delta_{QRS}}, \overline{\alpha})$. One regression function of the form

$$g(\overline{\Delta_{QRS}}, \overline{\alpha}) = \sum_{i=0}^{N}\sum_{j=0}^{N} \beta_{i,j} \left(\overline{\Delta_{QRS}}\right)^i (\overline{\alpha})^j + \varepsilon \tag{13}$$

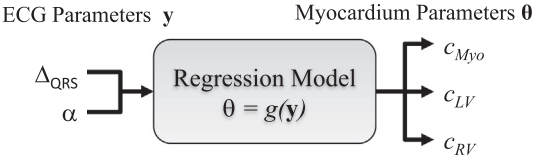

Fig. 6. Schematic diagram of the data-driven backward ECG model.

Table 2
Diffusion coefficient configurations for normalization forward runs.

Configuration	Diffusion coefficients (mm²/s)		
	c_{Myo}	c_{LV}	c_{RV}
F_1	100	4900	4900
F_2	100	100	4900
F_3	100	4900	100

is learned for each diffusivity parameter independently, $\mathbf{g} = (g_{Myo}, g_{LV}, g_{RV})$. During training, the regression coefficients $\beta_{i,j}$ are determined using QR decomposition such that the data is explained with minimal error ε. During testing, the diffusivity parameters are estimated for unseen data using measured and normalized ECG features:

$$\begin{pmatrix} \widehat{c_{Myo}} \\ \widehat{c_{LV}} \\ \widehat{c_{RV}} \end{pmatrix} = \begin{bmatrix} g_{Myo} \\ g_{LV} \\ g_{RV} \end{bmatrix} \begin{pmatrix} \overline{\Delta_{QRS}} \\ \bar{\alpha} \end{pmatrix} \tag{14}$$

2.4. Implementation

The strictly local stream-and-collide rules of the LBM-EP algorithm are inherently node-wise and can be implemented very efficiently in a single kernel on a GPU architecture. We use NVIDIA CUDA,[1] version 5.5, as our development environment. As shown by Georgescu et al. (2013), the simulation of transmembrane and extracellular potentials for a complete heart cycle on a Cartesian grid with an isotropic resolution of 1.5 mm only requires ≈ 3 s on an NVIDIA GeForce GTX 580 graphics card. The boundary element solver relies on the C++ Eigen library (Guennebaud et al., 2010). Training of and prediction with the regression model was performed using the MATLAB and Statistics Toolbox Release 2013b (MathWorks, Inc.).

3. Experiments and results

Before evaluating the method, clinical acceptance criteria were defined. In a study by Surawicz et al. (2009), the normal range for QRS duration in adult males was found to be between 74 and 114 ms (average 95 ms). Investigating intra-patient variability in electrocardiograms, Michaels and Cadoret (1967) defined the maximum permissible day-to-day difference in QRS duration as 20 ms. We assume predictions of QRS durations to be successful if within this range. The electrical axis, which is dependent on age and body physiology, is considered to be normal within −30° and 90°. A rough rule-based diagnosis scheme is often applied in clinical

[1] Compute Unified Device Architecture, http://developer.nvidia.com/cuda-toolkit.

routine. Left axis deviation, for instance, is present if lead I is positive and aVF is negative. Because such a scheme divides the QRS front plane in sectors of no less than 30°, prediction of the electrical axis was assumed to be successful if within this range.

3.1. Evaluation of the proposed forward model

A quantitative evaluation of the proposed forward model was carried out to understand model behavior but also to identify the optimal numerical parameters. For an extensive analysis of the LBM-EP solver, the reader is referred to Rapaka et al. (2012). The following sections therefore focus on the mapping of cardiac potentials onto the body surface and on the impact of EP parameters on the computed ECG.

3.1.1. Quantitative evaluation and convergence analysis of torso mapping

For the evaluation of the boundary element mapping from the epicardium to the torso, we chose a setup where an analytical solution to Eq. (8) exists. Both epicardium and torso were assumed to be concentric spheres, with radii r_H for the heart sphere and r_B for the body sphere. If not stated otherwise, Gaussian quadrature of order 37 was used. Homogeneous material between the two surfaces was also assumed. Using a spherical coordinate system with θ as the polar angle to the Cartesian z-direction and φ as the azimuth angle in the x–y-plane (Fig. 7a), we defined the extracellular potentials on the heart surface: $\phi_e(\theta,\varphi) = \cos(\theta)$ mV. Then, the potentials on the body ϕ_B were given as:

$$\phi_B(\theta,\varphi) = \frac{3}{2}\cos(\theta)\frac{1}{\frac{r_H}{r_B} + \frac{r_B^2}{2r_H^2}}\ \text{mV} \tag{15}$$

Fig. 7b illustrates the mapped potentials on the body sphere. In the reported experiments, $r_H = 100$ mm to roughly represent the human heart. Fig. 8a reports computed and analytical body potentials throughout a body sphere with $r_B = 300$ mm. Mapping to different body spheres (see Table 3 for mesh resolution details) showed that the algorithm was able to correctly compute the potentials at various distances (Fig. 8b). Absolute errors were on average $4.1 \cdot 10^{-5} \pm 1.4 \cdot 10^{-4}$ mV (mean ± standard deviation), far below the clinical acceptance threshold.

A convergence analysis with respect to the mesh resolution (Fig. 8c) indicated that with around 1500 mesh vertices (average edge length 31.7 mm for $r_B = 300$ mm) the ratio between BEM-based and analytical solutions is 99.70%, which relates to an absolute error of on average $9.3 \cdot 10^{-4}$ mV and is below the sensitivity of ECG sensors. For subsequent experiments, we therefore choose a similar resolution of 30–35 mm for the torso mesh. Similarly, the relative error also converged with increasing order of Gaussian quadrature as expected (Fig. 8d, experiments conducted with highest resolution mesh). Yet, low orders already reached a high degree of precision. The following experiments were therefore carried out with an order of 6, which showed to be a good compromise between accuracy and runtime performance (more than 6× as fast as highest order under consideration).

3.1.2. Parameter evaluation of complete forward model

Understanding the input parameters and output feature space of a given model is crucial before applying machine learning techniques and performing predictions. Therefore, we evaluated the influence of the most important parameters of our forward model on the ECG features under consideration. On a representative patient case, the dependence of QRS duration Δ_{QRS} and electrical axis α on diffusivity c, action potential duration (APD; governed by τ_{close}) and fiber elevation angle $\angle f$ was studied. In the following experiments, each of these parameters was varied, while the other parameters were fixed to their nominal value as given in Table 1 and 2.

First, the forward model was run with myocardium diffusion c_{Myo} ranging from 100 to 1000 mm^2/s, LV and RV diffusivity were fixed. As illustrated in Fig. 9a, and as expected, the QRS duration showed linear dependence on c_{Myo}. After an initial drop, the electrical axis stabilized when $c_{Myo} > 400$ mm^2/s. In total, the range of α in this experiment accounted for 92.9°. This behavior was not surprising, because the electrical axis was entirely governed by LV and RV endocardium diffusion at very low c_{Myo} values. As c_{Myo} increased, the effect of the Purkinje model was complemented by the fast myocardial diffusivity and the electrical axis value depended mostly on the geometrical configuration of the heart, i.e. its shape and relative position in the torso.

c_{Myo} was then fixed while the endocardial diffusion (c_{LV}, c_{RV}) was varied between 100 and 4900 mm^2/s with the constraint $c_{LV} + c_{RV} = 5000$ mm^2/s. As illustrated in Fig. 9b, an almost linear dependence of the electrical axis on endocardial diffusion was observed. This was also expected, as diffusion differences in the Purkinje fibers intuitively change the depolarization pattern. When c_{LV} and c_{RV} were similar ($|c_{LV} - c_{RV}| < 1000$ mm^2/s), the depolarization was controlled by the Purkinje system, and a small range of 8.6 ms was observed for the QRS duration. Either c_{LV} or c_{RV} approaching a bundle branch block scenario and thus becoming closer to myocardial diffusion, the QRS duration increased. The total range of Δ_{QRS} was found to be 35.8 ms.

Next, the influence of different spatial distributions of τ_{close} parameters, which control action potential duration, was investigated. The employed linear transmural gradient of action potential duration (Glukhov et al., 2010) was compared to a model with M-cells as described by Wilson et al. (2011). Hereby, we assumed M-cells to be located in the center of the myocardial wall, $\tau_{close_{mid}} = 110\% \cdot \tau_{close_{endo}}$ and performed linear interpolation between endocardium and M-cells, and between M-cells and epicardium to obtain a spatially varying map of τ_{close} values. For both scenarios (linear gradient throughout the wall and the M-cell model), we defined the parameter r_T as the ratio between the

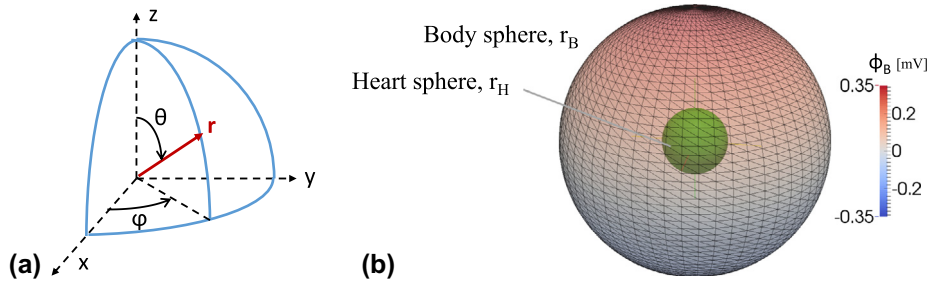

Fig. 7. (a) Definition of spherical coordinate system. (b) Heart sphere (green) and body sphere (semi-transparent) with mapped potentials ϕ_B. (For interpretation of the references to color in this figure legend, the reader is referred to the web version of this article.)

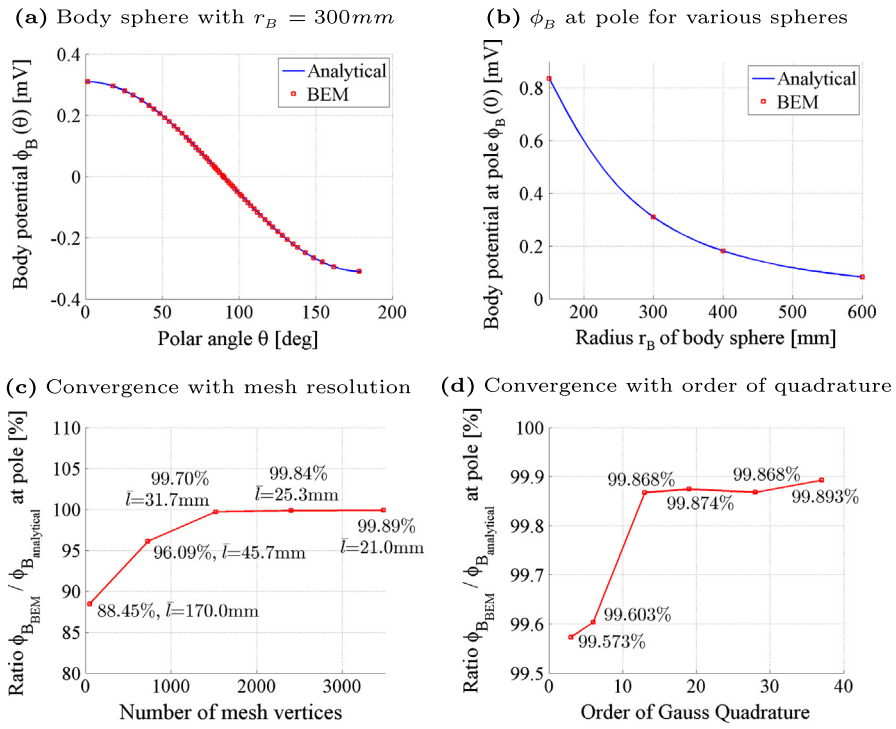

Fig. 8. Evaluation of BEM torso mapping. (a) Potentials throughout a body sphere with $r_B = 300$ mm and (b) potentials at the pole ($\theta = 0$, location of maximum error) for various body spheres (Table 3) matched the analytical solution. (c) Ratio between BEM-based and analytical solution for various mesh resolutions and average edge lengths $\bar{l}$, (d) and for various orders of Gaussian quadrature, showing that the method converges rapidly with increasing mesh resolution and order of quadrature.

Table 3
Body spheres used for torso mapping evaluation. See text for details.

Radius r_B (mm)	Number of vertices	Avg. edge length $\bar{l}$ (mm)
150	3482	10.5
300	3482	21.0
400	3482	28.0
600	3482	42.0

APD parameters at epicardium and endocardium: $r_T = \tau_{close_{epi}} / \tau_{close_{endo}}$. Fig. 10a shows that the difference in the considered ECG features between the linear gradient model and the used M-cell model was marginal. This result was not surprising as τ_{close} controls cardiac repolarization, whereas the QRS duration and electrical axis depend mostly on cardiac depolarization. Furthermore, we also analyzed how regional differences in APD can influence the ECG parameters. To that end, we created a base-to-apex gradient by defining an additional ratio $r_{BA} = \tau_{close_{base}} / \tau_{close_{apex}}$. In Fig. 10b, the resulting variation in Δ_{QRS} and α is illustrated. In this case, QRS duration was, as expected, only minimally affected (range 0.15 ms) but the electrical axis varied by 13.6°.

Finally, we investigated the effect of the fiber model on the ECG features. According to the study by Lombaert et al. (2012), fiber angles in human physiology range on average from about 50° to 80° on the epicardium. As shown in Fig. 11, the variation of Δ_{QRS} in that range was small, with a range of 8.2 ms. The electrical axis varied by 30.8° as the electrical activation pattern was modified due to the anisotropic diffusivity. However, that variation was still within the clinical range.

Altogether, these finding – linear dependence of Δ_{QRS} on myocardial diffusion, and linear dependence of α on LV/RV endocardial diffusion – confirmed the assumptions made in Section 2.2.3 and justified the selection of the two features for the estimation of cardiac electrical diffusivity. However, as expected, the experiments also showed that multiple combinations of c_{Myo}, c_{LV} and c_{RV} can yield the same set of ECG features. The resulting uncertainty of diffusion parameters given a set of ECG features will be quantified in Section 3.2.2. Because variation for different APD distributions and fiber elevation angles was found to be relatively low or cannot be directly measured in vivo at the time of this study, we focused on the estimation of diffusion coefficients, keeping the other parameters at their nominal value.

3.1.3. Analysis of computational efficiency

Using one representative patient case, computational efficiency was analyzed on a system with a 16-core Intel Xeon 64-bit CPU at 2.4 GHz and an NVIDIA GeForce GTX 580 graphics card. As described by Zettinig et al. (2013b), the computational times of image preparation and anatomical model creation, which has to be computed only once per patient, amounted to a total of 81.2 s. Table 4 reports the runtimes of the LBM-EP algorithm for a full heart cycle on differently spaced Cartesian grids (Georgescu et al., 2013). The projection of the extracellular potentials to the torso and the calculations of the ECG traces are simple matrix operations. Hence, the evaluation of the complete forward model could be done in less than 3 s for a grid with an isotropic resolution of 1.5 mm. As the evaluation of a polynomial function is almost immediate, the estimation of cardiac diffusivity required less than 10 s because of the three forward runs for the purpose of normalization.

3.2. Evaluation of the proposed data-driven estimation framework

3.2.1. Experimental protocol

In this study, datasets of 19 patients with dilated cardiomyopathy (DCM) and a QRS duration of at least 120 ms were used. For all of them, an anatomical model was created based on cine magnetic resonance images (MRI) as described in Section 2.1. Thereafter, 500 EP simulations were computed for each patient on a 1.5 mm-isotropic Cartesian grid, accounting for a total of 9500 forward model runs. Diffusivity coefficients were uniformly sampled

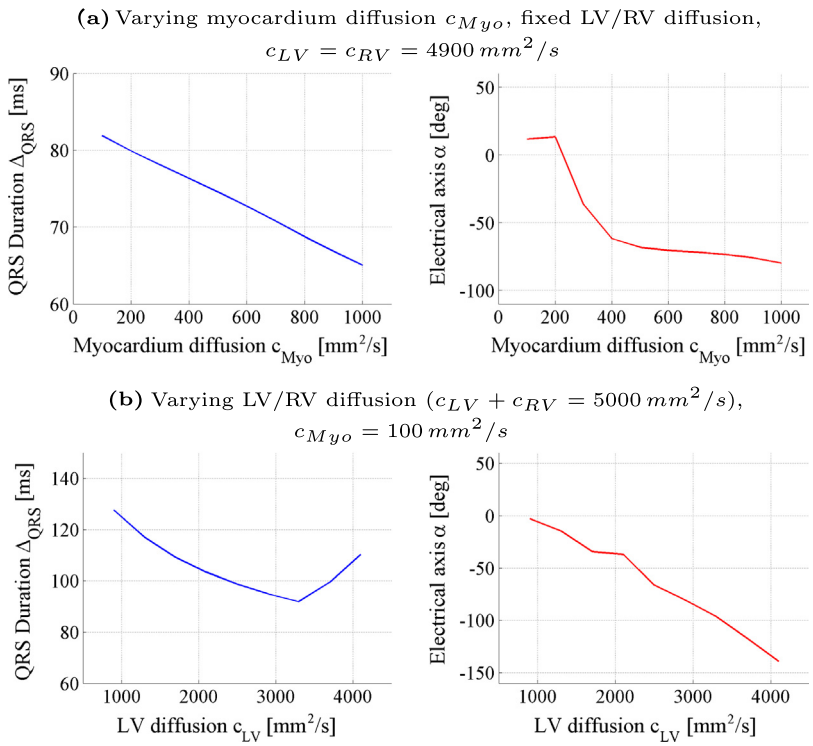

Fig. 9. Influence of diffusivity coefficients on ECG features. (a) QRS duration was linearly dependent on myocardium diffusion when LV and RV diffusion were fixed. Electrical axis varied little except for very low myocardium diffusion. (b) Electrical axis was almost linearly dependent on LV/RV diffusion when myocardium diffusion was fixed. QRS duration varied little except for low LV or RV diffusion (< 1500 mm²s, borders of plot).

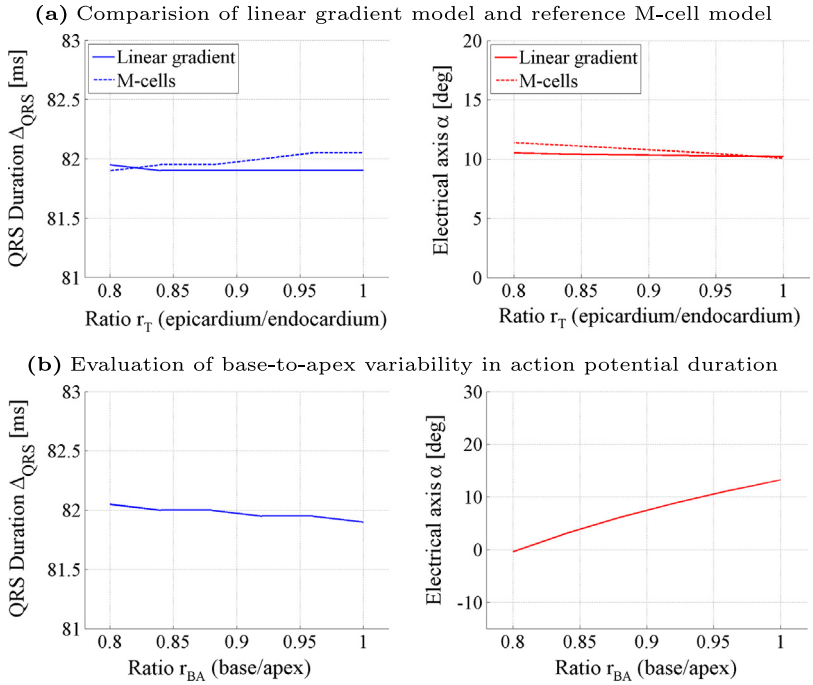

Fig. 10. Influence of action potential duration (τ_{close}) on ECG features. (a) The difference between the used linear gradient model and an M-cell model is negligible; the transmural ratio does not seem to significantly influence QRS duration and electrical axis. (b) A downward gradient (base to apex) only causes slight variation in ECG features, showing that regional differences in τ_{close} cause low variation in ECG features. See text for details.

between 50 mm²/s and 5000 mm²/s under the constraints $c_{Myo} \leqslant c_{LV}$ and $c_{Myo} \leqslant c_{RV}$.

3.2.2. Uncertainty analysis in cardiac diffusion parameters

Before training the regression model, the intrinsic uncertainty of the ECG inverse problem under our forward model was quantified using the entire synthetic EP database (9500 simulations). To minimize the effects of geometry, the analysis was conducted with normalized ECG parameters. All computed $(\overline{\Delta_{QRS}}, \overline{\alpha})$ tuples were grouped in 20×20 bins, and for each bin, the local standard deviation of the diffusion coefficients c_{Myo}, c_{LV} and c_{RV} was calculated. Table 5 reports the total standard deviation in the entire dataset,

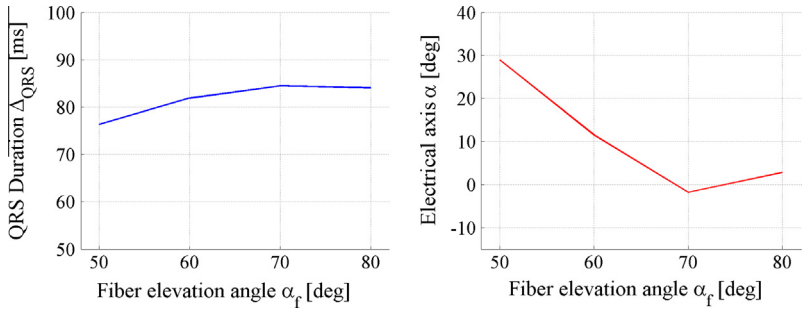

Fig. 11. Influence of fiber elevation angle α_f within physiological range on ECG features (the anatomical models are generated with α_f on the endocardium and $-\alpha_f$ on the epicardium).

Table 4
Full heart cycle runtimes of the LBM-EP algorithm for different grid spacings (Georgescu et al., 2013).

Grid spacing (mm)	GPU runtime (s)
1.5	2.8
0.7	21.7

the average local standard deviation, and the uncertainty defined as their ratio. As illustrated in Fig. 12, which shows the uncertainty for each bin, the highest variation can be found in the healthy range of QRS duration and electrical axis (up to 180%). The reported high uncertainties, especially for c_{LV} and c_{RV}, reflects the ill-posed nature of the ECG inverse problem if only QRS duration and electrical axis are employed to personalize the model. That information will be useful when evaluating the accuracy of the personalization techniques in the next sections.

3.2.3. Evaluation on synthetic data

The proposed machine-learning personalization procedure was evaluated using a leave-one-patient-out cross-validation on the database, i.e. the regression models were trained using a subset of 18 patients and tested with the remaining one, for each of the 19 DCM cases respectively. Next, the average testing errors in the diffusion (parameter) space were calculated. To evaluate the accuracy of the regression model in the observable space of ECG parameters, Δ_{QRS} and α were computed according to the estimated diffusivity parameters and quantitatively compared with the known ground truth. In order to analyze the required dimensionality of the polynomial regression model, a cross-validation procedure with regression degrees ranging from 1 to 8 was performed. While linear or quadratic regression models failed to capture the ECG problem, as shown in Fig. 13, the model started to overfit at degrees higher than four, leading to again increasing prediction errors in ECG space. Thus, the best option is to use cubic regression.

In Table 6, the final regression coefficients $\beta_{i,j}$ according to Eq. 13, trained using the entire synthetic dataset, are given. In Fig. 14, the regressed surfaces for each of the diffusion parameters are visualized. Myocardial diffusion c_{Myo} is, as expected, almost exclusively dependent on the QRS duration. Interestingly, for long QRS durations ($\overline{\Delta_{QRS}} \geq 1.7$), c_{RV} *decreases* for left axis deviations while still remaining higher than c_{LV}. Nevertheless, axis deviations on both sides are correctly captured, i.e. c_{RV} is clearly smaller than c_{LV} for deviations to the right, and c_{LV} is slightly smaller than c_{RV} for deviations to the left. Beyond the highlighted normalization range, all three polynomials may drop below zero for certain combinations of QRS duration and electrical axis, yielding non-physical diffusion coefficients. A test after the prediction can be used to discard these cases. The errors in estimated diffusion reported in Table 7 were obtained using this model. The relative errors in % of the total standard deviation of the dataset were in the same range as the estimated uncertainty of the inverse problem (Section 3.2.2). The proposed regression model was thus able to predict up to the intrinsic uncertainty of the problem. Furthermore, prediction errors were significantly higher when no normalization was applied, as illustrated in Table 7, suggesting the proposed model-based normalization procedure was able to partially compensate for inter-patient geometry variability.

Table 5
Total, and average local (bin-wise) standard deviation, and the uncertainty defined as their ratio for all three diffusion coefficients.

	c_{Myo}	c_{LV}	c_{RV}
Total SD (mm^2/s)	1482	1095	1191
Avg. local SD (mm^2/s)	191	556	537
Uncertainty (%)	12.9	50.7	45.1

In addition to the diffusion parameters used in the forward model (c_{Myo}, c_{LV} and c_{RV}), we tested how well the ratio between c_{LV}/c_{RV} can be reconstructed. Low prediction errors as listed in Table 7 were expected in light of the experiments carried out in the previous section, which showed a linear dependency of the electrical axis on c_{LV} when $c_{LV} + c_{RV}$ is kept constant. However, the ratio alone is not sufficient for a complete model personalization as the two values are needed.

Comparison against nominal values. Table 8 reports the average absolute errors in ECG feature space for forward model simulations with nominal diffusion parameters from literature and parameters obtained with the proposed regression framework. Likewise, the error distributions are shown in Fig. 15. Calibrated simulations using our framework were not only in the range of clinical variability but also significantly (t-test p-value < 0.001) more precise than those obtained with nominal diffusivity values. In addition, our predictions were on average centered around the ground truth QRS duration (average bias: +0.7 ms), the Δ_{QRS} calculated with default parameters was on average 28.9 ms too short. As the default parameters correspond to healthy physiology whereas conduction abnormalities cause prolonged QRS durations, this result was expected. Using our diffusion estimation framework may thus be preferable to using nominal parameters when only ECG is available.

Comparison against alternative machine learning techniques. In this study, the predictive power of the proposed polynomial regression framework is compared against two non-parametric non-linear methods: multivariate adaptive regression splines (MARS) and Gradient Boosting, as described in Hastie et al. (2009). The former, MARS, is a non-parametric regression method with explicative capabilities, which intuitively extends linear regression by fitting splines to the predictors to capture data non-linearities and variable interactions. For our evaluation, the ARESLab toolbox (Jekabsons, 2011) was used. Gradient Boosting,

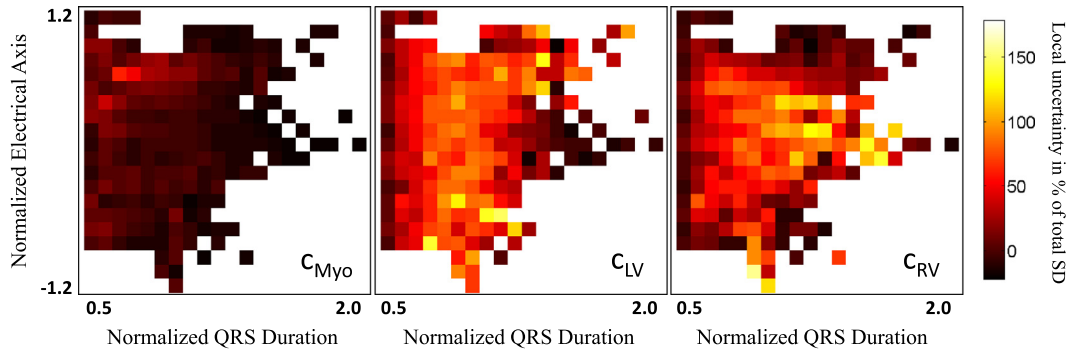

Fig. 12. Estimated diffusion standard deviation (SD) in % of total SD for known electrical axis and QRS duration. The highest uncertainty is found in the healthy range of parameters (center of plots).

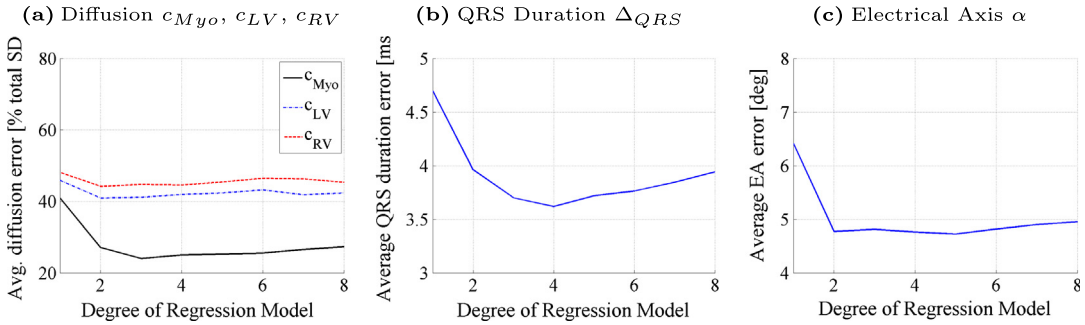

Fig. 13. Analysis of polynomial regression degree on prediction accuracy. Average testing errors of leave-one-patient-out cross-validation in (a) diffusion space, (b) QRS duration Δ_{QRS}, and (c) electrical axis α. The regression model overfits at degrees ≥ 4, as the prediction errors in ECG feature space increase again.

Table 6
Learned regression coefficients β_{ij} rounded to 5th decimal position (Eq. (13), Δ_{QRS} and α to be given in seconds and radians, respectively). Full double-precision coefficients are available from supplementary material.

i	j	g_{Myo}	g_{LV}	g_{RV}
3	0	−4397.72303	−2224.80345	−2372.28284
2	1	947.10794	−217.53110	−111.83210
2	0	20619.61231	8748.58856	10659.98012
1	2	−339.47629	884.12470	−1849.11181
1	1	−2138.03900	−556.40419	1168.22703
1	0	−31323.62564	−13516.54750	−15836.31353
0	3	−125.51341	−238.65933	513.65578
0	2	688.60647	−215.02537	1004.99532
0	1	1070.11229	585.32229	−900.63528
0	0	15662.21934	9621.33473	10454.35893

Table 7
Diffusion space prediction errors on the synthetic dataset, absolute in mm^2/s and relative in % of the total standard deviation. In addition to the three parameters, also the ratio between c_{LV} and c_{RV} was tested.

	c_{Myo}	c_{LV}	c_{RV}	c_{LV}/c_{RV}
With Normalization	356	451	533	
	24.0%	41.2%	44.7%	21.3%
Without normalization	571	540	597	
	38.5%	49.3%	50.0%	23.9%

on the other hand, is based on an ensemble of weak prediction models, in our case 100 decision trees (LSBoost function of MATLAB). Table 9 lists the diffusion space errors for all tested machine learning algorithms. The errors in ECG feature space can be found in Table 8 and Fig. 15. Both approaches yielded very similar diffusion error distributions compared to the proposed polynomial regression framework. Also the error distributions of Δ_{QRS} and α obtained by MARS and Gradient Boosting were similar to those obtained by polynomial regression.

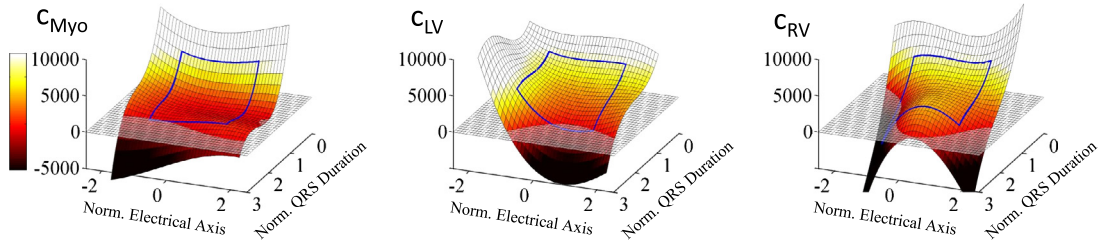

Fig. 14. Regressed surface for each diffusion parameter. The highlighted area (blue contour) corresponds to the normalized parameter range in Fig. 12. As expected, all three parameters are dependent on the QRS duration, and the electrical axis has little effect on c_{Myo}. Right axis deviations correctly lead to $c_{RV} < c_{LV}$, and vice versa. Beyond the normalization range, all polynomials may drop below zero (non-physical diffusivity) for certain parameter combinations. *See text for details.* (For interpretation of the references to color in this figure legend, the reader is referred to the web version of this article.)

Table 8
Average absolute ECG feature space errors for ECG simulations with nominal, NEWUOA-estimated and predicted diffusivity parameters using a machine learning technique.

Diffusivity	Δ_{QRS} (ms)	α (deg)
Nominal parameters	33.7 ± 15.7	53.2 ± 33.8
NEWUOA optimization	7.4 ± 11.3	16.1 ± 31.4
MARS	4.6 ± 5.1	9.8 ± 23.0
Gradient boosting	4.9 ± 5.8	9.5 ± 19.8
Polynomial regression	4.8 ± 6.0	8.9 ± 19.7

Comparison against an alternative inverse-problem method. We compared the performance of the regression framework with a personalization approach that is based on NEWUOA (Powell, 2006, 2008), a gradient-free inverse problem method. An algorithm similar to the approach proposed by Neumann et al. (2014) is followed. The diffusion coefficients $c^0_{Myo}, c^0_{LV}, c^0_{RV}$ are initialized with parameters associated with healthy EP (Table 2, configuration F_1). The initial step size is set to 500 mm^2/s. Cardiac diffusivity is then estimated using NEWUOA such that both the QRS durations and the electrical axis match:

$$(c^*_{Myo}, c^*_{LV}, c^*_{RV}) = \underset{c_{Myo},c_{LV},c_{RV}}{\arg\min}\, C\left[f_{\Delta_{QRS},\alpha}(c_{Myo}, c_{LV}, c_{RV})\right] \tag{16}$$

Hereby, $f_{\Delta_{QRS},\alpha}(\cdot)$ denotes the ECG features obtained by running the EP forward model. In the cost function C, the values Δ^m_{QRS} and α^m are the measured QRS duration and electrical axis, respectively, and the parameter $\lambda = 0.1$ accounts for the different orders of magnitude between QRS duration (in seconds) and electrical axis (in radians):

$$C(\Delta^i_{QRS}, \alpha^i) = |\Delta^m_{QRS} - \Delta^i_{QRS}| + \lambda|\alpha^m - \alpha^i| \tag{17}$$

As shown in Table 8, the errors in Δ_{QRS} and α calculated using the NEWUOA-personalized forward model were higher compared to the data-driven estimation framework. In addition, the obtained values for the electrical axis were less centered around the ground truth (average bias: 8.1°). Note that the table lists higher standard deviations (11.3 ms and 31.4° for Δ_{QRS} and α, respectively) than Fig. 15 suggests because of numerous outliers (16%) in the NEWUOA predictions.

Because the optimizer was sensitive to local minima, NEWUOA typically required up to 50 iterations to converge to a stable optimum. Thus, the total time for optimization using a fully optimized version of the code would take up to 2.5 min, while our approach requires only 10 s to calculate the three forward simulations for the normalization. Our approach was therefore not only at least 15× more computationally efficient but also yielded more predictive diffusivity parameters.

Table 9
Diffusion space prediction errors on the synthetic dataset, relative in % of the total standard deviation, for the tested machine learning algorithms.

	c_{Myo} (%)	c_{LV} (%)	c_{RV} (%)
MARS	23.2	40.2	43.7
Gradient boosting	24.3	46.1	49.1
Polynomial regression	24.0	41.2	44.7

3.2.4. Evaluation on real DCM cases

Finally, we evaluated the machine-learning personalization with the clinical ECG data which were available for all 19 DCM cases. The trained regression models from the cross-validation were employed to estimate diffusion coefficients based on measured QRS duration and electrical axis. In three cases, the prediction was not successful and yielded negative diffusivity for at least one of the diffusion parameters because the measured electrical axis was outside the normalization range. These cases are easily identifiable and could therefore be processed using other approaches if needed. For the remaining 16 patients, plausible diffusion coefficients (between 141 and 582 mm^2/s for c_{Myo}, and between 678 and 2769 mm^2/s for c_{LV} and c_{RV}) were estimated. Table 10 reports the average absolute errors between clinical ground truth and ECG features obtained with forward model computations using the estimated diffusion parameters for the remaining 16 patients. Fig. 16 shows the obtained error distributions, indicating that the simulated QRS duration was on average 18 ms too long, while the electrical axis was closely centered (average bias: 3.1°) around the measurements, both values being within clinical acceptability as defined prior to the study. Finally, Fig. 17 illustrates the simulated ECG chest leads overlaid on the measured ones for one representative patient.

4. Discussion and conclusions

4.1. Discussion

In this paper, we described a data-driven method for the personalization of a cardiac electrophysiology model from ECG features. As supported by reported results, the method achieves the same accuracy as traditional inverse problem algorithm with the advantage of (1) being computationally efficient (evaluation of a polynomial function is almost immediate) and (2) providing an estimate of parameter uncertainty, an additional variable that could be employed clinically.

While the anatomical model was obtained from cine MR images in this work, the approach is easily applicable to other modalities such as computed tomography (CT) or echocardiography

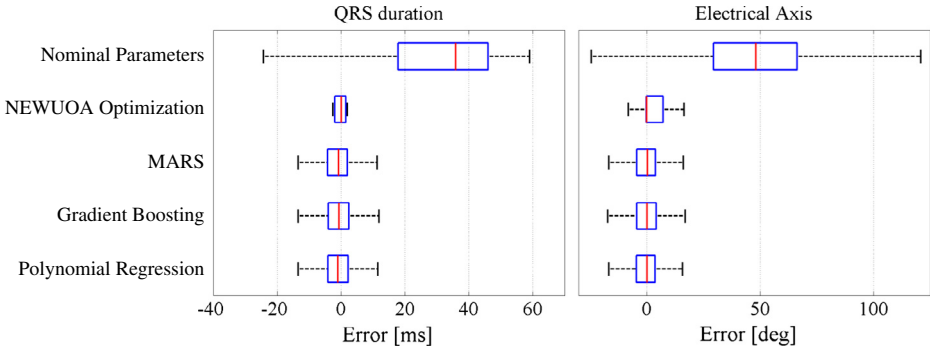

Fig. 15. QRS duration and electrical axis error distributions for ECG simulations with nominal, NEWUOA-estimated and predicted diffusivity parameters using a machine learning technique. On each box, the central mark is the median, the edges of the box are the quartiles, and the whiskers extend to the most extreme data points not considered outliers. The range between the whiskers covers approximately 99.3% of the normally distributed data.

Table 10
Average absolute ECG feature space errors for ECG computations with regression-predicted diffusivity parameters from clinically measured ECG features.

Diffusivity	Δ_{QRS} (ms)	α (deg)
Regression-based prediction	18.7 ± 16.2	6.5 ± 7.6

(Zheng et al., 2008), provided the full bi-ventricular myocardium is visible. In this study, a synthetic model of fiber architecture was employed. Nevertheless, our framework is ready to incorporate diffusion tensor imaging (DTI) data and thus remove this additional uncertainty. It will be important to quantify the difference between ex-vivo measurements (Helm et al., 2005) and in vivo measurements in order to learn a data-driven model for patient-specific diffusivity predictions. Furthermore, it would be interesting to investigate how the variances of the atlas generated by Lombaert et al. (2012) can be used for a sensitivity analysis and uncertainty estimation in our model. In any case, the tremendous progress achieved in in vivo DTI will soon enable to use patient-specific data (Toussaint et al., 2013). For the mapping of potentials onto the body surface, an atlas of torso geometry was employed as 3D images of patient upper body were not available. The manual registration of the atlas against 2D contours outlined in the three sagittal, axial and longitudinal planes was performed by an expert. It should be noted however that slight mis-registration would not have impacted the performance of the algorithm as ECG leads are known to be tolerant with respect to electrode placement (Sheppard et al., 2011). In addition, the overall methodology would work on more detailed atlases based on populations or on the patient-specific geometry directly.

This work was performed using a mono-domain EP model with the action potential model proposed by Mitchell and Schaeffer (2003). It has been shown by Boulakia et al. (2010) and Plank et al. (2013) that anisotropic mono-domain models are able to preserve the essential ECG features, which were used for the subsequent personalization, when compared to orthotropic bi-domain models. It should be noted that the LBM-EP method can use any mono-domain model like for instance the TenTusscher model. Furthermore, the data-driven personalization algorithm is generic by design and can be applied to any cell model, or any bi-domain or graph-based/Eikonal model of cardiac electrophysiology, as far as the database can be computed in a realistic amount of time. Moreover, our focus on cardiac depolarization allowed decoupling the estimation of electrical diffusivity from repolarization EP parameters and assuming a static heart. Unlike during the ST-T period, the deformation of the myocardium due to cardiac motion has been shown to be marginal during the QRS complex (Jiang et al., 2009). Also, the influence of the action potential duration on the ECG features used to estimate electrical diffusion (QRS duration and electrical axis) was confirmed to be negligible (Fig. 10).

In this study, the mapping of extracellular potentials from the heart to the body surface relies on a boundary element approach. For our simulations, we applied constant homogeneous isotropic conductivity in the torso, including the chest cavity, thoracic cage, muscle tissue and skin. Minor sensitivity on body surface potentials for different organ conductivities as observed in the computational study by Geneser et al. (2008) justifies this assumption for our purposes. We verified our BEM implementation with analytically defined test cases and showed convergence with increasing mesh resolution and order of Gaussian quadrature for the evaluation of integrals without available closed-form formula (Fig. 8), suggesting that the uncertainty in diffusivity parameters is not related to BEM numerical approximations but rather intrinsic to the inverse ECG problem.

From the ECG traces, two features were derived, namely the QRS duration Δ_{QRS} and the electrical axis α. Provided the choice of appropriate electrode positions, experiments have shown that the electrical axis can be computed on either the epicardium mesh or the torso mesh. A thorough evaluation of the influence of varying conductivities in the torso due to different organs (Geneser et al., 2008) onto the electrical axis measured at the torso would be interesting for future works. Regarding the computation of the QRS duration, we observed in our experiments a close match between the duration computed directly using the LBM-EP results as described in Section 2.2.3 and the width of the QRS complex in the computed ECG leads. This work is based on the assumption that these two features are sufficient to explain various EP patterns. In addition, the selected features are commonly available from clinical ECG traces and clinical reports, and would therefore

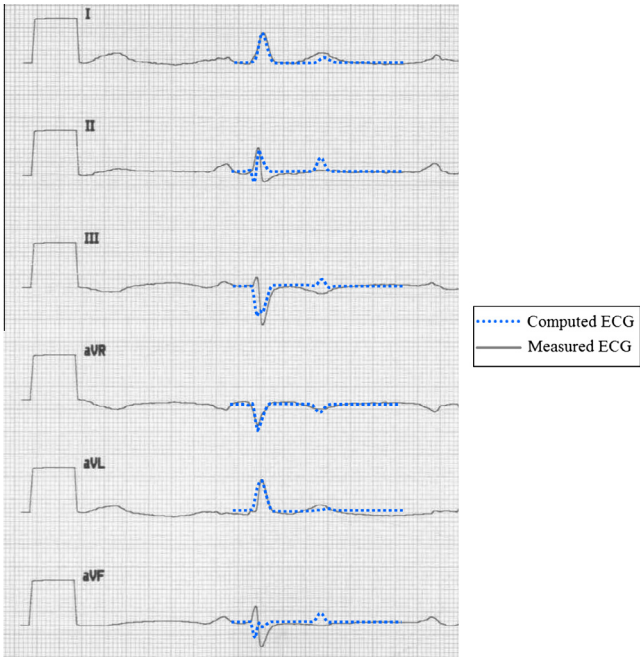

Fig. 17. Clinically measured, and computed ECG chest leads after model estimation of cardiac diffusivity for one representative patient, showing promising agreement during cardiac depolarization, which we focused on in this study. For this case, obtained estimation errors amounted to 1.6 ms for the QRS duration and 0.5° for the electrical axis.

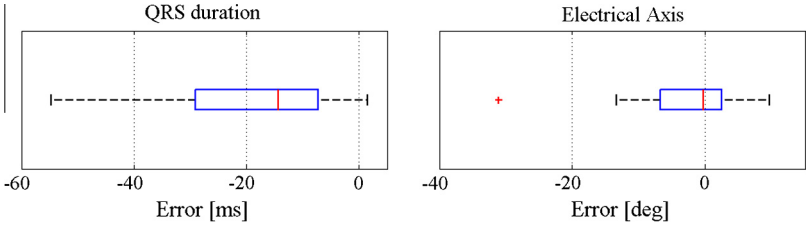

Fig. 16. QRS duration and electrical axis error distributions for ECG simulations diffusivity parameters estimated from clinical ground truth measurements.

allow the estimation of diffusion coefficients with little effort in clinical routine. The proposed method could therefore constitute a first model personalization step when no dense EP data is available, and would also provide more accurate results compared to generic parameters, as suggested by our experiments. Yet, the proposed framework is generic and allows the integration of an arbitrary number of features. If invasive or BSM measurements are available, more regional features could be used to facilitate the estimation of model parameters.

The use of QRS duration and electrical axis was further supported by our parameter analysis. It has been shown in this paper that QRS duration varies linearly with myocardial diffusion (c_{Myo}), while the electrical axis varies linearly with increasing left endocardial diffusion (c_{LV}) when the right endocardial diffusion (c_{RV}) is decreased at the same time such that their sum is constant. However, these relationships are not decoupled as each diffusion parameter has influence on both features, which contributes to the quantified uncertainty of the inverse problem: different diffusivity configurations can lead to the same ECG parameters. In particular, we showed that left and right endocardial diffusivity are subject to broad variations, especially in the region of healthy EP (Fig. 12). Clearly demonstrating the ill-posed nature of the inverse ECG problem under the assumptions of our EP model, the reported uncertainties constitute, to the best of our knowledge, the first estimates of the optimal bound in accuracy for any inverse problem to estimate myocardium diffusion that rely on Δ_{QRS} and α only. We expect the uncertainty to decrease as more clinical features are considered. This study is thus subject to future work.

The main contribution of this work is our novel data-driven framework to estimate cardiac diffusion parameters. Instead of solving the inverse ECG problem numerically, we proposed to employ statistical learning, and in particular multivariate polynomial regression, to learn the relationship between ECG features and diffusivity. Compared to other statistical approaches, polynomial regression has the advantage that the regression coefficients can be given and the estimation of diffusion parameters is possible using a closed-form formula. The personalization formula can therefore be shared between research groups. Error distributions obtained using multivariate adaptive regression splines (MARS) and Gradient Boosting were, as reported in Table 8, similar to those obtained by polynomial regression. An evaluation of the required polynomial degree revealed that the model starts over-fitting at degree 4 (Fig. 13). We therefore use cubic multivariate regression and report the final coefficients in Table 6.

A key aspect of the approach is the model-based normalization of EP features to indirectly incorporate geometric information in the statistical model. The strategy consists in scouting the space of Δ_{QRS} and α for a given patient by running three forward simulations with diffusion parameters relating to healthy EP, and left and right bundle branch block scenarios. As a result, although not directly based on anatomical or physiological features such as heart size or strength of myocardial contraction, we were able to show that the normalization scheme compensates for patient geometry and significantly improves prediction results (Table 7). For an unseen patient, three forward model runs are needed (computed in about 10 s using LBM-EP), which is still acceptable in a clinical setting but also far less than in conventional inverse-problem algorithms, which require often numerous model evaluations to converge.

As expected, the regressed surfaces of the three diffusivities trained from a database of 9500 simulations (Fig. 14) showed dependance of the QRS duration on all three diffusion parameters. For right axis deviations, the right endocardial diffusion was consistently lower than the left one, and vice versa. However, all three polynomials may yield negative, non-physical diffusion coefficients for certain parameter combinations. As not reported, preliminary experiments have shown, regressing the logarithm of the diffusion coefficients (log c instead of c directly) could help in overcoming this limitation. Future work will therefore consider the investigation of regression methods with better generalization on unseen data. Prediction errors in diffusion space (leave-one-patient-out) were in the range of the estimated intrinsic uncertainty of the problem, especially for left and right endocardial diffusivity (Table 7). Only for myocardial diffusivity, the prediction was slightly worse (24% of total std. dev.) compared to the uncertainty (13% of total std. dev.) One reason for this result could be the dependence of myocardial diffusivity on both ECG features for diffusions of less than 400 mm^2/s (Fig. 9a).

Yet, prediction errors in the ECG feature space for the synthetic dataset obtained by running forward simulations using the calibrated EP model were significantly better than those obtained by using nominal diffusion parameters from literature (Table 8). Furthermore, a comparison with an estimation algorithm based on the gradient-free inverse problem method NEWUOA showed that our method performs better (prediction errors in QRS duration and electrical axis were 54% and 80% higher, respectively) while being immediate to compute and providing uncertainty estimates. Altogether, the application of the proposed data-driven framework may thus be preferential to traditional approaches when only ECG data are available.

Finally, an evaluation with clinically measured ECG features was conducted on all 19 patient cases. The model was successfully fitted in 16 cases out of 19 (84%), with promising prediction errors of 18.7 ± 16.2 ms for Δ_{QRS} and $6.5 \pm 7.6^\circ$ for α, within clinical acceptability. The model could not be personalized in three cases as the measured electrical axis was outside the normalization range. Similar results were obtained in not reported, preliminary experiments on regressing the logarithm of the diffusion coefficients, as mentioned above. However, the cases that failed could not be recovered either, suggesting a more intrinsic difference between patient physiology and our model, for instance a potential line of blocks, etc. A more realistic incorporation of geometrical features might improve the success rate and avoid such inconsistencies. Further investigation is needed for an optimal regression model.

The results previously published by Zettinig et al. (2013a) showed smaller overall errors in Δ_{QRS} and α, potentially because (1) fewer patients with a smaller range of anatomical and physiological variation were used, and (2) the original framework (multivariate polynomial regression of degree 7) might have been overfitting as shown in Fig. 13. In addition, estimation errors without normalization were better than previously reported, possibly due to the updated torso registration technique.

4.2. Perspectives

In this work, only the cardiac anatomy model was generated based on patient data. Despite the contour-based registration, torso geometry was based on an atlas and does not entirely reflect patient-specific anatomy. Also the boundary element mapping of potentials assumes constant conductivity, neglecting thoracic organs and different tissue types. Future work could thus improve the anatomical model by incorporating more imaging data from the heart to the body surface and model the different tissues in the torso independently (lung, bones, muscles). Furthermore, instead of the proposed normalization technique, explicitly integrating geometrical features directly into the regression framework could potentially better cope with anatomical variability. In addition, the framework could be extended by using an electromechanical model of the heart (Zettinig et al., 2013b) to cope with the influence of cardiac motion on the ECG. A comprehensive study is needed though to quantify that aspect and properly con-

sider it into the estimation process. There are indeed no studies available to clarify how much motion happens during the fast depolarization of the heart, to the best of our knowledge. Even though, a dynamic model would have great benefit when estimated cardiac repolarization features like action potential duration.

As the uncertainty in diffusion parameters given QRS duration and electrical axis is high, the integration of more ECG features could improve estimation precision and increase the success rate of the approach. Similarly, more ECG features may potentially allow the estimation of more local diffusion coefficients, rendering the estimation of regional diffusivity distributions possible.

Finally, refining the forward model, in particular regarding cardiac electrophysiology, might lead to future extensions of our framework. More complex biophysical bi-domain models, integration of atrial geometry, more refined activation patterns, and coupling with mechanical models could potentially increase the predictive power of the framework and are subject to future work.

4.3. Conclusion

We have shown in this paper that the estimation of patient-specific cardiac diffusion parameters from standard 12-lead ECG measurements using machine learning techniques is possible, up to the intrinsic uncertainty of the problem. Based on QRS duration and electrical axis as ECG features, a data-driven regression model was trained and used to predict diffusivity parameters for left and right endocardium (mimicking the fast conducting Purkinje system), and the bulk myocardium tissue. Under the assumptions of our forward model, the prediction errors were in the range of the underlying uncertainty in diffusivity, which we empirically quantified for the first time to the best of our knowledge. We evaluated the framework both on the synthetic dataset and on clinical measurements using a leave-one-patient-out cross-validation and computed the error in ECG feature space using forward simulations with estimated diffusion parameters. Significant improvement with respect to nominal diffusivity values, which relate to healthy electrophysiology, were obtained. We also conducted a comparison with a NEWUOA-based personalization approach, finding overall superior predictive power. Therefore, our framework can provide good preliminary personalization, prior to more refined estimation if invasive or BSM measurements are available.

Appendix A. Supplementary material

Supplementary data associated with this article can be found, in the online version, at http://dx.doi.org/10.1016/j.media.2014.04.011.

References

Aliev, R.R., Panfilov, A.V., 1996. A simple two-variable model of cardiac excitation. Chaos Solitons Fract. 7, 293–301.

Arsigny, V., Fillard, P., Pennec, X., Ayache, N., 2006. Log-euclidean metrics for fast and simple calculus on diffusion tensors. Magn. Reson. Med. 56, 411–421.

Auricchio, A., Prinzen, F.W., et al., 2011. Non-responders to cardiac resynchronization therapy: the magnitude of the problem and the issues. Circ. J.: Off. J. Jpn. Circ. Soc. 75, 521–527.

Barr, R.C., Ramsey, M., Spach, M.S., 1977. Relating epicardial to body surface potential distributions by means of transfer coefficients based on geometry measurements. IEEE Trans. Biomed. Eng. 24, 1–11.

Bayer, J., Blake, R., Plank, G., Trayanova, N., 2012. A novel rule-based algorithm for assigning myocardial fiber orientation to computational heart models. Ann. Biomed. Eng. 40, 2243–2254.

Boulakia, M., Cazeau, S., Fernández, M.A., Gerbeau, J.F., Zemzemi, N., 2010. Mathematical modeling of electrocardiograms: a numerical study. Ann. Biomed. Eng. 38, 1071–1097.

Bourgault, Y., Coudière, Y., Pierre, C., 2009. Existence and uniqueness of the solution for the bidomain model used in cardiac electrophysiology. Nonlinear Anal.: Real World Appl. 10, 458–482.

Chhay, M., Coudière, Y., Turpault, R., 2012. How to Compute the Extracellular Potential in Electrocardiology from an Extended Monodomain Model. Research Report RR-7916. INRIA.

Chinchapatnam, P., Rhode, K.S., Ginks, M., Rinaldi, C.A., Lambiase, P., Razavi, R., Arridge, S., Sermesant, M., 2008. Model-based imaging of cardiac apparent conductivity and local conduction velocity for diagnosis and planning of therapy. IEEE Trans. Med. Imaging 27, 1631–1642.

Chung, E.K., 1989. Comprehensive electrocardiography: theory and practice in health and disease. JAMA: J. Am. Med. Assoc. 262, 571.

Clayton, R., Panfilov, A., 2008. A guide to modelling cardiac electrical activity in anatomically detailed ventricles. Prog. Biophys. Mol. Biol. 96, 19–43.

Clayton, R., Bernus, O., Cherry, E., Dierckx, H., Fenton, F., Mirabella, L., Panfilov, A., Sachse, F., Seemann, G., Zhang, H., 2011. Models of cardiac tissue electrophysiology: progress, challenges and open questions. Prog. Biophys. Mol. Biol. 104, 22–48.

Coudière, Y., Pierre, C., 2006. Stability and convergence of a finite volume method for two systems of reaction–diffusion equations in electro-cardiology. Nonlinear Anal.: Real World Appl. 7, 916–935.

Dössel, O., Krueger, M.W., Weber, F.M., Schilling, C., Schulze, W.H., Seemann, G., 2011. A framework for personalization of computational models of the human atria. In: Engineering in Medicine and Biology Society, EMBC, 2011 Annual International Conference of the IEEE. IEEE, pp. 4324–4328.

Fenton, F., Karma, A., 1998. Vortex dynamics in three-dimensional continuous myocardium with fiber rotation: filament instability and fibrillation. Chaos: Interdiscipl. J. Nonlinear Sci. 8, 20–47.

Ferri, F., 2013. Ferri's Clinical Advisor 2013. Elsevier Mosby.

FitzHugh, R., 1961. Impulses and physiological states in theoretical models of nerve membrane. Biophys. J. 1, 445–466.

Franzone, P.C., Guerri, L., Rovida, S., 1990. Wavefront propagation in an activation model of the anisotropic cardiac tissue: asymptotic analysis and numerical simulations. J. Math. Biol. 28, 121–176.

Geneser, S.E., Kirby, R.M., MacLeod, R.S., 2008. Application of stochastic finite element methods to study the sensitivity of ecg forward modeling to organ conductivity. IEEE Trans. Biomed. Eng. 55, 31–40.

Georgescu, B., Rapaka, S., Mansi, T., Zettinig, O., Kamen, A., Comaniciu, D., 2013. Towards real-time cardiac electrophysiology computations using GP-GPU Lattice-Boltzmann method. In: Proceedings of 6th International Workshop on High Performance Computing for Biomedical Image Analysis (HPC-MICCAI). Springer.

Glukhov, A.V., Fedorov, V.V., Lou, Q., Ravikumar, V.K., Kalish, P.W., Schuessler, R.B., Moazami, N., Efimov, I.R., 2010. Transmural dispersion of repolarization in failing and nonfailing human ventricle. Circ. Res. 106, 981–991.

Guennebaud, G., Jacob, B., et al., 2010. Eigen v3. <http://eigen.tuxfamily.org>.

Gulrajani, R.M., 1998. The forward and inverse problems of electrocardiography. Eng. Med. Biol. Mag. IEEE 17, 84–101.

Han, C., Pogwizd, S.M., Killingsworth, C.R., Zhou, Z., He, B., 2013. Noninvasive cardiac activation imaging of ventricular arrhythmias during drug-induced QT prolongation in the rabbit heart. Heart Rhythm 10, 1509–1515.

Hastie, T., Tibshirani, R., Friedman, J., 2009. The Elements of Statistical Learning: Data Mining, Inference, and Prediction. Springer.

Helm, P.A., Tseng, H.J., Younes, L., McVeigh, E.R., Winslow, R.L., 2005. Ex vivo 3D diffusion tensor imaging and quantification of cardiac laminar structure. Magn. Reson. Med. 54, 850–859.

Hodgkin, A.L., Huxley, A.F., 1952. A quantitative description of membrane current and its application to conduction and excitation in nerve. J. Physiol. 117, 500–544.

Jekabsons, G., 2011. ARESLab: Adaptive Regression Splines Toolbox for Matlab/Octave. <http://www.cs.rtu.lv/jekabsons/>.

Jiang, M., Xia, L., Shou, G., Wei, Q., Liu, F., Crozier, S., 2009. Effect of cardiac motion on solution of the electrocardiography inverse problem. IEEE Trans. Biomed. Eng. 56, 923–931.

Jiang, M., Lv, J., Wang, C., Huang, W., Xia, L., Shou, G., 2011. A hybrid model of maximum margin clustering method and support vector regression for solving the inverse ECG problem. In: Computing in Cardiology, 2011. IEEE, pp. 457–460.

Keener, J.P., Sneyd, J., 1998. Mathematical Physiology, vol. 8. Springer.

Konukoglu, E., Relan, J., Cilingir, U., Menze, B.H., Chinchapatnam, P., Jadidi, A., Cochet, H., Hocini, M., Delingette, H., Jaïs, P., et al., 2011. Efficient probabilistic model personalization integrating uncertainty on data and parameters: application to eikonal-diffusion models in cardiac electrophysiology. Prog. Biophys. Mol. Biol. 107, 134–146.

Li, Z., Zhu, S., He, B., 2007. Solving the ECG forward problem by means of a meshless finite element method. Phys. Med. Biol. 52, N287.

Liu, C., Eggen, M.D., Swingen, C.M., Iaizzo, P.A., He, B., 2012. Noninvasive mapping of transmural potentials during activation in swine hearts from body surface electrocardiograms. IEEE Trans. Med. Imaging 31, 1777–1785.

Lombaert, H., Peyrat, J., Croisille, P., Rapacchi, S., Fanton, L., Cheriet, F., Clarysse, P., Magnin, I., Delingette, H., Ayache, N., 2012. Human atlas of the cardiac fiber architecture: Study on a healthy population. IEEE Trans. Med. Imaging 31, 1436–1447.

Luo, C.h., Rudy, Y., 1991. A model of the ventricular cardiac action potential. Depolarization, repolarization, and their interaction.. Circ. Res. 68, 1501–1526.

Marcus, G.M., Keung, E., Scheinman, M.M., 2013. The year in review of cardiac electrophysiology. J. Am. Coll. Cardiol. 61, 772–782.

McMurray, J.J., Adamopoulos, S., Anker, S.D., Auricchio, A., Böhm, M., Dickstein, K., Falk, V., Filippatos, G., Fonseca, C., Gomez-Sanchez, M.A., et al., 2012. ESC guidelines for the diagnosis and treatment of acute and chronic heart failure 2012. Eur. Heart J. 33, 1787–1847.

Mendis, S., Puska, P., Norrving, B., 2011. Global Atlas on Cardiovascular Disease Prevention and Control. World Health Organization.

Michaels, L., Cadoret, R., 1967. Day-to-day variability in the normal electrocardiogram. Br. Heart J. 29, 913–919.

Mitchell, C.C., Schaeffer, D.G., 2003. A two-current model for the dynamics of cardiac membrane. Bull. Math. Biol. 65, 767–793.

Modre, R., Tilg, B., Fischer, G., Wach, P., 2002. Noninvasive myocardial activation time imaging: a novel inverse algorithm applied to clinical ecg mapping data. IEEE Trans. Biomed. Eng. 49, 1153–1161.

Moireau, P., 2008. Assimilation de données par filtrage pour les systèmes hyperboliques du second ordre-Applications à la mécanique cardiaque. Ph.D. thesis, Ecole Doctorale de l'Ecole Polytechnique, Paris.

Neumann, D., Mansi, T., Grbic, S., Voigt, I., Georgescu, B., Kayvanpour, E., Amr, A., Sedaghat-Hamedani, F., Haas, J., Katus, H., Meder, B., Hornegger, J., Kamen, A., Comaniciu, D., 2014. Automatic image-to-model framework for patient-specific electromechanical modeling of the heart, in: IEEE International Symposium on Biomedical Imaging (in press).

Noble, D., 1962. A modification of the Hodgkin–Huxley equations applicable to Purkinje fibre action and pacemaker potentials. J. Physiol. 160, 317–352.

Noble, D., Varghese, A., Kohl, P., Noble, P., 1998. Improved guinea-pig ventricular cell model incorporating a diadic space, IKr and IKs, and length-and tension-dependent processes. Can. J. Cardiol. 14, 123.

Pernod, E., Sermesant, M., Konukoglu, E., Relan, J., Delingette, H., Ayache, N., 2011. A multi-front eikonal model of cardiac electrophysiology for interactive simulation of radio-frequency ablation. Comput. Graph. 35, 431–440.

Plank, G., Costa, C.M., Prassl, A.J., 2013. Parametrization strategies for matching activation sequences in models of ventricular electrophysiology. In: Engineering in Medicine and Biology Society (EMBC), 2013 35th Annual International Conference of the IEEE. IEEE, pp. 1534–1537.

Potse, M., Dubé, B., Richer, J., Vinet, A., Gulrajani, R.M., 2006. A comparison of monodomain and bidomain reaction–diffusion models for action potential propagation in the human heart. IEEE Trans. Biomed. Eng. 53, 2425–2435.

Potse, M., Dubé, B., Vinet, A., 2009. Cardiac anisotropy in boundary-element models for the electrocardiogram. Med. Biol. Eng. Comput. 47, 719–729.

Powell, M., 2006. The NEWUOA software for unconstrained optimization without derivatives. In: Pillo, G., Roma, M. (Eds.), Large-Scale Nonlinear Optimization, Nonconvex Optimization and Its Applications, vol. 83. Springer, US, pp. 255–297.

Powell, M.J., 2008. Developments of NEWUOA for minimization without derivatives. IMA J. Numer. Anal. 28, 649–664.

Prakosa, A., Sermesant, M., Allain, P., Villain, N., Rinaldi, C., Rhode, K., Razavi, R., Delingette, H., Ayache, N., 2013. Cardiac electrophysiological activation pattern estimation from images using a patient-specific database of synthetic image sequences. IEEE Trans. Biomed. Eng. 61, 235–245.

Rapaka, S., Mansi, T., Georgescu, B., Pop, M., Wright, G.A., Kamen, A., Comaniciu, D., 2012. LBM-EP: Lattice–Boltzmann method for fast cardiac electrophysiology simulation from 3D images. Medical Image Computing and Computer-Assisted Intervention – MICCAI 2012. LNCS, vol. 7511. Springer, pp. 33–40.

Relan, J., Chinchapatnam, P., Sermesant, M., Rhode, K., Ginks, M., Delingette, H., Rinaldi, C.A., Razavi, R., Ayache, N., 2011. Coupled personalization of cardiac electrophysiology models for prediction of ischaemic ventricular tachycardia. Interface Focus 1, 396–407.

Roger, V.L., Go, A.S., Lloyd-Jones, D.M., Benjamin, E.J., Berry, J.D., Borden, W.B., Bravata, D.M., Dai, S., Ford, E.S., Fox, C.S., et al., 2012. Executive summary: heart disease and stroke statistics – 2012 update: a report from the american heart association. Circulation 125, 188–197.

Sermesant, M., Konukoglu, E., Delingette, H., Coudière, Y., Chinchapatnam, P., Rhode, K.S., Razavi, R., Ayache, N., 2007. An anisotropic multi-front fast marching method for real-time simulation of cardiac electrophysiology. Functional Imaging and Modeling of the Heart. LNCS, vol. 4466. Springer, pp. 160–169.

Sermesant, M., Billet, F., Chabiniok, R., Mansi, T., Chinchapatnam, P., Moireau, P., Peyrat, J.M., Rhode, K., Ginks, M., Lambiase, P., et al., 2009. Personalised electromechanical model of the heart for the prediction of the acute effects of cardiac resynchronisation therapy. Functional Imaging and Modeling of the Heart. LNCS, vol. 5528. Springer, pp. 239–248.

Sethian, J.A., 1999. Level Set Methods and Fast Marching Methods: Evolving Interfaces in Computational Geometry, Fluid Mechanics, Computer Vision, and Materials Science, vol. 3. Cambridge University Press.

Sheppard, J.P., Barker, T.A., Ranasinghe, A.M., Clutton-Brock, T.H., Frenneaux, M.P., Parkes, M.J., 2011. Does modifying electrode placement of the 12 lead ecg matter in healthy subjects? Int. J. Cardiol. 152, 184–191.

Shou, G., Xia, L., Jiang, M., Wei, Q., Liu, F., Crozier, S., 2009. Solving the ECG forward problem by means of standard H- and H-hierarchical adaptive linear boundary element method: comparison with two refinement schemes. IEEE Trans. Biomed. Eng. 56, 1454–1464.

Surawicz, B., Childers, R., Deal, B.J., Gettes, L.S., 2009. AHA/ACCF/HRS recommendations for the standardization and interpretation of the electrocardiogram, Part III: intraventricular conduction disturbances a scientific statement from the american heart association electrocardiography and arrhythmias committee, council on clinical cardiology; the american college of cardiology foundation; and the heart rhythm society endorsed by the international society for computerized electrocardiology. J. Am. Coll. Cardiol. 53, 976–981.

Talbot, H., Marchesseau, S., Duriez, C., Sermesant, M., Cotin, S., Delingette, H., 2013. Towards an interactive electromechanical model of the heart. Interface Focus 3, 20120091.

Ten Tusscher, K., Noble, D., Noble, P., Panfilov, A., 2004. A model for human ventricular tissue. Am. J. Physiol.-Heart Circ. Physiol. 286, H1573–H1589.

Toussaint, N., Stoeck, C.T., Sermesant, M., Schaeffter, T., Kozerke, S., Batchelor, P.G., 2013. In-vivo human cardiac fibre architecture estimation using shape-based diffusion tensor processing. Med. Image Anal. 17, 1243–1255.

Van Oosterom, A., Strackee, J., 1983. The solid angle of a plane triangle. IEEE Trans. Biomed. Eng. 30, 125–126.

Wallman, M., Smith, N.P., Rodriguez, B., 2012. A comparative study of graph-based, eikonal, and monodomain simulations for the estimation of cardiac activation times. IEEE Trans. Biomed. Eng. 59, 1739–1748.

Wallman, M., Smith, N.P., Rodriguez, B., 2014. Computational methods to reduce uncertainty in the estimation of cardiac conduction properties from electroanatomical recordings. Med. Image Anal. 18, 228–240.

Wang, L., Wong, K.C., Zhang, H., Liu, H., Shi, P., 2011. Noninvasive computational imaging of cardiac electrophysiology for 3-d infarct. IEEE Trans. Biomed. Eng. 58, 1033–1043.

Wilson, L.D., Jennings, M.M., Rosenbaum, D.S., 2011. Point: M cells are present in the ventricular myocardium. Heart Rhythm 8, 930–933.

Wu, M.T., Su, M.Y.M., Huang, Y.L., Chiou, K.R., Yang, P., Pan, H.B., Reese, T.G., Wedeen, V.J., Tseng, W.Y.I., 2009. Sequential changes of myocardial microstructure in patients postmyocardial infarction by diffusion-tensor cardiac MR correlation with left ventricular structure and function. Circ.: Cardiovasc. Imaging 2, 32–40.

Zettinig, O., Mansi, T., Georgescu, B., Kayvanpour, E., Sedaghat-Hamedani, F., Amr, A., Haas, J., Steen, H., Meder, B., Katus, H., Navab, N., Kamen, A., Comaniciu, D., 2013a. Fast data-driven calibration of a cardiac electrophysiology model from images and ECG. Medical Image Computing and Computer-Assisted Intervention – MICCAI 2013. LNCS, vol. 8149. Springer, pp. 1–8.

Zettinig, O., Mansi, T., Georgescu, B., Rapaka, S., Kamen, A., Haas, J., Frese, K.S., Sedaghat-Hamedani, F., Kayvanpour, E., Amr, A., Hardt, S., Mereles, D., Steen, H., Keller, A., Katus, H.A., Meder, B., Navab, N., Comaniciu, D., 2013b. From medical images to fast computational models of heart electromechanics: an integrated framework towards clinical use. Functional Imaging and Modeling of the Heart. LNCS, vol. 7945. Springer, pp. 249–258.

Zheng, Y., Barbu, A., Georgescu, B., Scheuering, M., Comaniciu, D., 2008. Four-chamber heart modeling and automatic segmentation for 3-D cardiac CT volumes using marginal space learning and steerable features. IEEE Trans. Med. Imaging 27, 1668–1681.